



저작자표시-비영리-변경금지 2.0 대한민국

이용자는 아래의 조건을 따르는 경우에 한하여 자유롭게

- 이 저작물을 복제, 배포, 전송, 전시, 공연 및 방송할 수 있습니다.

다음과 같은 조건을 따라야 합니다:



저작자표시. 귀하는 원저작자를 표시하여야 합니다.



비영리. 귀하는 이 저작물을 영리 목적으로 이용할 수 없습니다.



변경금지. 귀하는 이 저작물을 개작, 변형 또는 가공할 수 없습니다.

- 귀하는, 이 저작물의 재이용이나 배포의 경우, 이 저작물에 적용된 이용허락조건을 명확하게 나타내어야 합니다.
- 저작권자로부터 별도의 허가를 받으면 이러한 조건들은 적용되지 않습니다.

저작권법에 따른 이용자의 권리는 위의 내용에 의하여 영향을 받지 않습니다.

이것은 [이용허락규약\(Legal Code\)](#)을 이해하기 쉽게 요약한 것입니다.

[Disclaimer](#)

공학박사학위논문

**Optimal Trajectory Generation and Robust Control  
of a Launch Vehicle during Asecnt Phase**

상승단계 발사체의 최적 궤적 생성 및 강건 제어 기법

2018년 2월

서울대학교 대학원

기계항공공학부

김 승 현

Optimal Trajectory Generation and Robust Control  
of a Launch Vehicle during Ascent Phase

상승단계 발사체의 최적 궤적 생성 및 강건 제어 기법

지도교수 김 현 진

이 논문을 공학박사 학위논문으로 제출함

2017년 6월

서울대학교 대학원

기계항공공학부

김 승 현

김승현의 공학박사 학위논문을 인준함

2017년 6월

위원장: 김 유 안

부위원장: 김 현 진

위원: 백 권 국

위원: 박 민 제

위원: 김 승 환



**Optimal Trajectory Generation and Robust Control  
of a Launch Vehicle during Ascent Phase**

A Dissertation

by

Seunghyun Kim

Presented to the Faculty of the Graduate School of  
Seoul National University  
in Partial Fulfillment  
of the Requirements  
for the Degree of

DOCTOR OF PHILOSOPHY

Department of Mechanical and Aerospace Engineering

Seoul National University

Supervisor : Professor H. Jin Kim

February 2018

**Optimal Trajectory Generation and Robust Control  
of a Launch Vehicle during Ascent Phase**

Seunghyun Kim

Department of Mechanical and Aerospace Engineering

Seoul National University

APPROVED:



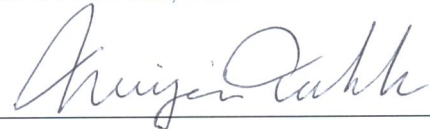
Youdan Kim, Chair, Ph.D.




H. Jin Kim, Ph.D.



Chan Gook Park, Ph.D.



Min-Jea Tahk, Ph.D.



Seung-Hwan Kim, Ph.D.

*to my*

*MOTHER, FATHER, and SISTER*

*with love*

## Abstract

# Optimal Trajectory Generation and Robust Control of a Launch Vehicle during Ascent Phase

Seunghyun Kim

Department of Mechanical and Aerospace Engineering

The Graduate School

Seoul National University

This research focused on trajectory generation and control of a flexible launch vehicle during ascent flight. An important issue of a launch vehicle design is generating optimal trajectory during its atmospheric ascent flight while satisfying constraints such as aerodynamic load. These constraints become more significant due to wind disturbance, especially in the maximum dynamic pressure region. On the other hand, modern launch vehicles are becoming long and slender for the reduction in structure mass to increase payload. As a result, they possess highly flexible bending modes in addition to aerodynamically unstable rigid body characteristics.

This dissertation proposes a rapid and reliable optimization approach for trajectory generation via sequential virtual motion camouflage (VMC) and non-conservative robust control for an unstable and flexible launch vehicle.

First, an optimal trajectory is generated in a rapid and reliable manner through the introduction of the virtual motion camouflage. VMC uses an observed biological phenomenon called motion camouflage to construct a subspace in which the solution trajectory is generated. By the virtue of this subspace search, the overall dimension of the optimization problem is reduced, which decreases the computational time significantly compared to a traditional direct input programming.

Second, an interactive optimization algorithm is proposed to find a feasible solution

easier. For this, the constraint correction step is added after VMC optimization. Since VMC is a subspace problem, a feasible solution may not exist when subspace is not properly constructed. In order to address this concern, a quadratic programming (QP) problem is formulated to find a direction along which the parameters defining the subspace can be improved. Via a computationally fast QP, specific parameters (such as prey and reference point) used in VMC can be refined quickly and sequentially. As a result, the proposed interactive optimization algorithm is less sensitive to the initial guess of the optimization parameters.

Third, a non-conservative 2-DOF  $H_\infty$  controller for an unstable and flexible launch vehicle is proposed. The objectives of the control system are to provide sufficient margins for the launch vehicle dynamics and to enhance the speed of the closed-loop response. For this, a robust control approach is used. The key of the control design is to overcome conservativeness of the robust control. The baseline controllers using the optimal control such as LQG and LQI are designed prior to a robust controller. These optimal controllers are used to find a desirable shape of the sensitivity transfer function in order to reduce conservativeness of the robust control. After implementation and analysis of the baseline controllers, an improved sensitivity weighting function is defined as a non-conventional form with different slopes in the low frequency and around crossover frequency, which results in performance enhancement without loss of robustness. A two-degree-of-freedom  $H_\infty$  controller is designed which uses feedback and feedforward control together to improve tracking performance with the proposed sensitivity weighting function as a target closed-loop shape. The resulting  $H_\infty$  controller stabilizes the unstable rigid body dynamics with sufficient margins in the low frequency, and also uses gain stabilization in addition to phase stabilization to handle the lightly damped bending modes in the high-frequency region.

**Keywords:** Launch vehicle, Optimal trajectory generation, Virtual motion camouflage (VMC), Robust control,  $H_\infty$  control

**Student Number:** 2013-30190



# Table of Contents

	<b>Page</b>
Abstract . . . . .	vi
Table of Contents . . . . .	viii
List of Tables . . . . .	xi
List of Figures . . . . .	xii
<b>Chapter</b>	
1 Introduction . . . . .	1
1.1 Background and motivations . . . . .	1
1.2 Literature survey . . . . .	3
1.2.1 Optimal trajectory generation for a launch vehicle . . . . .	3
1.2.2 Controller design for a flexible launch vehicle . . . . .	5
1.3 Research objectives and contributions . . . . .	6
1.4 Thesis organization . . . . .	7
2 Launch Vehicle Dynamics . . . . .	9
2.1 Frame and coordinate . . . . .	9
2.2 Rigid body motion . . . . .	9
2.3 Aerodynamic forces and moments . . . . .	12
2.4 Gravity force . . . . .	14
2.5 Thrust forces and moments . . . . .	14
2.6 Flexible bending modes . . . . .	15
3 Optimal Trajectory Generation . . . . .	16
3.1 VMC based trajectory optimization . . . . .	16
3.1.1 Nonlinear constrained trajectory optimization problem . . . . .	17
3.1.2 VMC formulation . . . . .	17

3.2	VMC based trajectory optimization applied to the launch vehicle . . . . .	21
3.2.1	Relationship between launch vehicle dynamics and VMC . . . . .	21
3.2.2	Selection of reference point and virtual prey motion . . . . .	23
3.2.3	Trajectory optimization via VMC . . . . .	25
3.2.4	Sequential VMC: constraint correction . . . . .	27
3.2.5	Comparison study . . . . .	29
3.3	Numerical simulations . . . . .	31
3.3.1	Case 1: No wind disturbance . . . . .	36
3.3.2	Case 2: $Z$ -axis wind disturbance . . . . .	39
3.3.3	Case 3: $Y$ -axis wind disturbance . . . . .	43
3.3.4	Case 4: $Z$ and $Y$ -axes wind disturbance . . . . .	48
3.3.5	Performance comparison . . . . .	51
4	Robust Control . . . . .	57
4.1	Launch vehicle model description . . . . .	57
4.1.1	Rigid body model . . . . .	58
4.1.2	Flexible modes and Actuator . . . . .	59
4.1.3	System properties and design specifications . . . . .	63
4.2	Baseline controllers design . . . . .	65
4.2.1	Set-point LQG . . . . .	65
4.2.2	Integral LQG . . . . .	69
4.3	Robust controller design . . . . .	74
4.3.1	$H_\infty$ control theory . . . . .	74
4.3.2	Two-degree-of freedom $H_\infty$ controller . . . . .	76
4.3.3	Selection of weighting functions: $W_p$ and $W_u$ . . . . .	77
4.3.4	Synthesis results . . . . .	82
4.3.5	Comparison study . . . . .	88
4.4	Numerical simulation . . . . .	94
5	Conclusions . . . . .	98

Abstract (*in Korean*) . . . . . 106

# List of Tables

3.1	Launch vehicle specifications . . . . .	32
3.2	Ascent phase mission . . . . .	33
3.3	VMC optimization results . . . . .	54
3.4	Direct input programming results . . . . .	55
3.5	Pseudospectral optimization results . . . . .	55
3.6	Comparison of cost and computational time . . . . .	55
4.1	The uncertainty range of the $i$ -th flexible bending mode . . . . .	60
4.2	Comparison of GM and PM . . . . .	93

# List of Figures

1.1	LV mission profile [1] . . . . .	2
1.2	Long and slender launch vehicle configurations . . . . .	3
1.3	Study logic . . . . .	8
2.1	Coordinate systems . . . . .	10
3.1	VMC concept . . . . .	18
3.2	Reference point and prey motion . . . . .	24
3.3	Aerodynamic load . . . . .	25
3.4	Sequential VMC, update of prey motion and reference point by improving direction 'd' . . . . .	30
3.5	Ascent phase mission . . . . .	32
3.6	Reference wind profile . . . . .	33
3.7	Trajectory comparison (RK4 and 20 nodes) . . . . .	34
3.8	Comparison of aerodynamic angles (RK4 and 20 nodes) . . . . .	35
3.9	Optimization results of case 1: No wind (using 20 nodes) . . . . .	37
3.10	Trajectory results of case 1: No wind . . . . .	38
3.11	Optimization results of case 2: $Z$ -axis wind (using 20 nodes) . . . . .	40
3.12	Trajectory result of case 2: $Z$ -axis wind (using 20 nodes) . . . . .	41
3.13	Trajectory results of case 2: various $Z$ -axis wind (using 20 nodes) . . . . .	41
3.14	Optimization results of case 2: various $Z$ -axis wind (using 20 nodes) . . . . .	42
3.15	Optimization results of case 3 : $Y$ -axis wind (using 20 nodes) . . . . .	44
3.16	Trajectory result of case 3: $Y$ -axis wind (using 20 nodes) . . . . .	45
3.17	Trajectory results of case 3: various $Y$ -axis wind (using 20 nodes) . . . . .	46
3.18	Optimization results of case 3: various $Y$ -axis wind (using 20 nodes) . . . . .	47

3.19	Optimization results of case 4: $Y$ , $Z$ -axes wind (using 20 nodes) . . . . .	49
3.20	Trajectory results of case 4: $Y$ , $Z$ -axes wind . . . . .	50
3.21	Optimization result comparison . . . . .	52
3.22	Trajectory comparison . . . . .	53
3.23	Comparison of results . . . . .	56
4.1	Launch vehicle model in the pitch plane . . . . .	58
4.2	Block diagram of the launch vehicle with the rigid body and flexible body parts . . . . .	60
4.3	Bode plot of the launch vehicle w/ and w/o actuator dynamics . . . . .	62
4.4	Root locus of the launch vehicle with actuator dynamics Eq. (4.7) . . . . .	64
4.5	General 2-DOF control structure . . . . .	65
4.6	Set-point LQG control structure . . . . .	66
4.7	Root locus of set-point LQG . . . . .	66
4.8	Simulation results of the set-point LQG . . . . .	68
4.9	LQI control structure . . . . .	69
4.10	Simulation results of the LQI with $PI_1$ . . . . .	71
4.11	Simulation results of the LQI with $PI_2$ . . . . .	73
4.12	Closed-loop system with uncertainty . . . . .	75
4.13	Controller synthesis framework . . . . .	75
4.14	Analysis framework . . . . .	76
4.15	2-DOF $H_\infty$ control structure with model reference . . . . .	77
4.16	2-DOF $H_\infty$ control structure augmented by $z_3$ . . . . .	79
4.17	Bode plot of the weighting functions . . . . .	81
4.18	Synthesis results of the 2-DOF $H_\infty$ with $W_{p1}$ and $W_{u1}$ . . . . .	84
4.19	Simulation results of the 2-DOF $H_\infty$ with $W_{p1}$ and $W_{u1}$ . . . . .	85
4.20	Synthesis results of the 2-DOF $H_\infty$ with $W_{p2}$ and $W_{u2}$ . . . . .	86
4.21	Simulation results of the 2-DOF $H_\infty$ with $W_{p2}$ and $W_{u2}$ . . . . .	87

4.22	Two-loop control structure . . . . .	88
4.23	Bode plot of two-loop controller . . . . .	90
4.24	Synthesis result of two-loop controller . . . . .	91
4.25	Comparison of step response . . . . .	92
4.26	Singular value plot of the gain-scheduled controller . . . . .	96
4.27	6-DOF simulation results . . . . .	97

# 1

## Introduction

### 1.1 Background and motivations

---

An important issue of a launch vehicle flight is generating optimal trajectory during its atmospheric ascent flight while satisfying constraints such as bending moment or altitude. These constraints are significantly influenced by wind disturbance, especially in the maximum dynamic pressure region. Generally, atmospheric ascent guidance is conducted as open-loop due to the difficulty of finding an analytic solution or real-time optimal guidance in the presence of aerodynamic forces and wind. Also, during the flight, attitude control system has to maintain the launch vehicle on the optimized trajectory by using thrust vector control (TVC).

As illustrated in Fig. 1.1, ascent flight of a launch vehicle starts from lift-off and lasts until the first stage separation. During this phase, the velocity of a launch vehicle increases to Mach 5.5 at an altitude of 57 km and time of 125 sec. An ascent flight trajectory can be separated into the vertical flight, and transition turn. After lift-off, the launch vehicle flies vertically and turns slowly toward the designated position by using TVC.



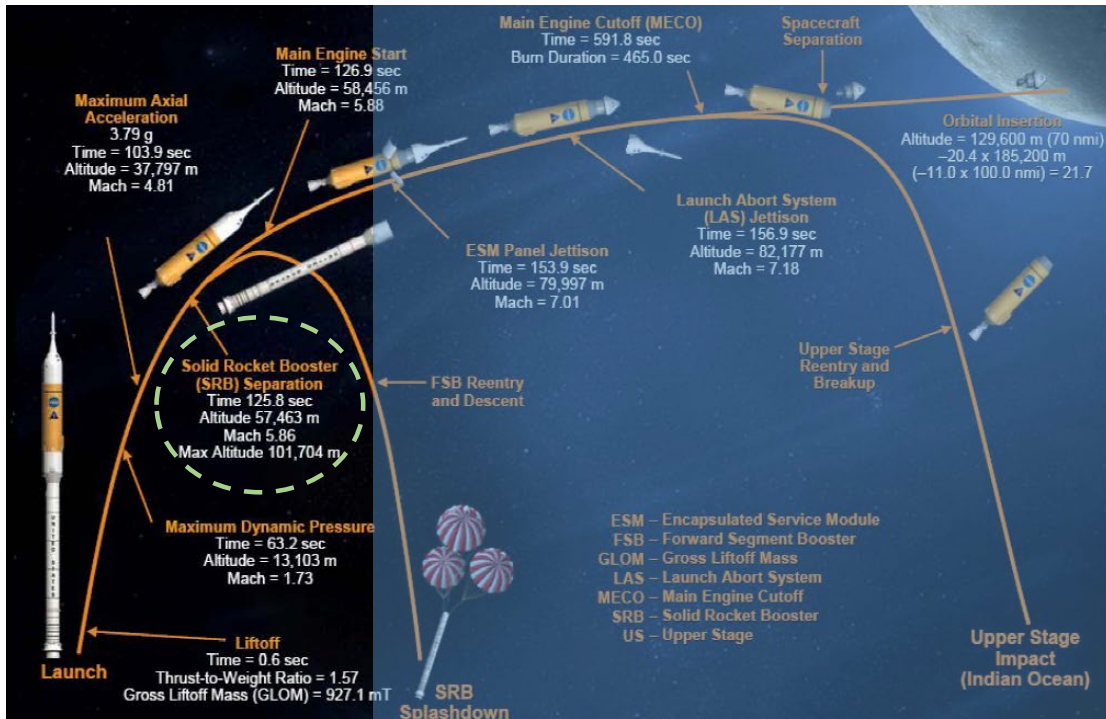


Figure 1.1: LV mission profile [1]

In this ascent phase, aerodynamic load management is very important because the high dynamics pressure region can cause a structural failure from the excessive bending moment. Therefore, the objective of the optimal trajectory generation should include minimization of the aerodynamic load while satisfying the designated position and velocity at the final time. Furthermore, fast computation time is desirable because a rapid trajectory optimization can allow trajectories to be generated minutes before launch, or allow reoptimization of the trajectory in flight.

On the other hand, modern launch vehicles are becoming long and slender for the reduction in structure mass to increase payload as shown in Fig. 1.2. As a result, they possess highly flexible bending modes in addition to aerodynamically unstable rigid body characteristics. In order to stabilize the unstable rigid dynamics, a feedback controller with a sufficient gain should be designed, but such control system has the potential to excite lightly damped poles of the flexible bending modes [2]. Furthermore, parameters defining



Figure 1.2: Long and slender launch vehicle configurations

the launch vehicle system such as unstable pole and natural frequencies of bending modes are highly uncertain. Therefore, one of the main challenges of a control system for the launch vehicle is to stabilize this unstable interaction in the presence of large uncertainty and disturbance. At the same time, sufficient response speed is also demanded.

## 1.2 Literature survey

---

This section offers the survey results of scholarly articles, books, and other sources relevant to this research. Since this dissertation consists of the two main topics, the related literatures are categorized into those : (i) Optimal trajectory generation for a launch vehicle, (ii) Controller design for a flexible launch vehicle.

### 1.2.1 Optimal trajectory generation for a launch vehicle

The dynamics of a launch vehicle considered in this work is nonlinear, and it has many constraints. Therefore, nonlinear constrained optimal approaches have to be conducted to

design the trajectory of a launch vehicle. Many numerical methods studied to solve an optimal trajectory problem of a launch vehicle [3, 4, 5, 6] can be divided into two categories as direct nonlinear programming (NLP) and indirect approaches with Pontryagin's minimum principle (PMP) [7].

In the indirect methods, a solution is derived from the calculus of variations, and a two-point-boundary-value problem (TPBVP) has to be solved for trajectory optimization. In [3], a multiple shooting method is used to enhance the convergence performance of the simple shooting method. In [8], an indirect finite element method is adopted to solve TPBVP of a launch vehicle. These methods usually provide quick convergence. However, the essential shortcoming is that the convergence property is extremely sensitive to the initial guess of costate.

On the other hand, nonlinear programming has been studied for direct optimization method [9, 10, 11, 12, 13]. In [11, 12], a Legendre pseudospectral method for a launch vehicle trajectory optimization is presented. There, the time domain of the trajectory is discretized at a special set of Legendre-Gauss-Lobato points and the pseudospectral differential matrix is used to find a derivative of discretized states. Due to this differential matrix, the number of discretized nodes can be reduced successfully, which results in relatively rapid optimization. However, the dimension of the problem is sometimes too large for rapid applications.

Recently, the idea of a motion camouflage (MC) strategy[14] is applied to the nonlinear constrained trajectory optimization problem, which is called virtual motion camouflage (VMC)[15, 16, 17]. Therein, the VMC method is used to reformulate the typical nonlinear constrained trajectory optimization problem by using path control parameter (PCP). Then, the optimization problem can be solved by optimizing PCPs. Due to this reformulation, the original dimension of the problem can be reduced, which makes the convergence faster and easier.

### 1.2.2 Controller design for a flexible launch vehicle

Much research has been conducted to design controllers for flexible launch vehicles [18, 19, 20, 21]. Within these work, adaptive control approaches such as L1 adaptive control [22, 23, 24] and adaptive notch filter [25, 26] have been employed in order to handle uncertainties in the flexible bending modes. While the adaptive control can handle the uncertainty well, relative stability such as gain margin and phase margin, and desired level of robustness is not guaranteed. Instead, frequency-domain synthesis techniques are more suitable to handle uncertain flexible bending modes in the high-frequency region by specifying roll-off characteristic [27]. For this reason, robust control synthesis such as  $H_\infty$  control has been applied to the launch vehicle control design [28].

Since conventional  $H_\infty$  synthesis imposes some conservatism, other robust control techniques such as  $\mu$ -synthesis [29, 30] and multi-objective control [31] have been developed. In [32, 33], the Youla-parameterization is used to define all stabilizing controllers, and the linear matrix inequalities (LMI) is used to specify different design objectives. In [34], the cross-standard form (CSF) technique is used in inverse optimal control after designing some baseline controller to satisfy performance requirement, and then the robustness requirement is added to this CSF system in the frequency domain.

On the other hand, a two-degree-of-freedom controller which uses both feedforward and feedback control can be used practically to achieve the performance such as response speed and robustness together[35]. In [36, 37], an original unstable plant is preliminarily stabilized before employing the standard robust control design process. This two-loop structure results in the two-degree-of-freedom control structure.

## 1.3 Research objectives and contributions

---

This dissertation deals with two main topics: (i) trajectory optimization (ii) robust control for a flexible launch vehicle. First, we propose a rapid and reliable optimization method for trajectory generation via sequential virtual motion camouflage. Second, a non-conservative robust controller is proposed for an unstable and flexible launch vehicle, which is achieved by designing an improved weighting function. The main contributions can be summarized as below.

- A rapid and reliable optimization method for trajectory generation of a launch vehicle is proposed through the introduction of the virtual motion camouflage (VMC). VMC uses the concept of prey motion and reference point motivated by a biological phenomenon called motion camouflage to construct a subspace in which the solution trajectory is generated. By the virtue of this subspace search, the overall dimension of the optimization problem is reduced, which decreases the computational time significantly compared to traditional direct input programming. Also, in the VMC approach, certain optimal parameters are calculated rather than optimized to satisfy equality boundary conditions. The fact that no equality constraints are involved in the optimization also makes the convergence easier. In contrast with the indirect method, the parameters to be optimized in the VMC approaches are physically meaningful and defining a reasonable initial guess is not difficult.
- An interactive optimization algorithm is proposed to find a feasible solution more accessible by adding the constraint correction step. Since the VMC is a subspace problem, a feasible solution may not exist when subspace is not properly constructed. In order to address this concern, a quadratic programming problem is formulated to find a direction along which the parameters defining the subspace can be improved. Via a computationally fast QP, certain parameters (prey and reference point) used in VMC can be refined quickly and sequentially. As a result, the proposed interactive

optimization algorithm is insensitive to initial guess of the optimization parameters.

- A non-conservative 2-DOF  $H_\infty$  controller for an unstable and flexible launch vehicle is proposed. The objectives of a control system are to provide sufficient margins for the launch vehicle dynamics and to enhance the speed of the closed-loop response. For this, a robust control approach is used. The key of the control design is targeted to overcome conservativeness of the robust control. It is found that the two-degree-of-freedom control structure which uses feedforward and feedback control together is suitable and effective for this kind of system. The baseline controllers are designed using the optimal control such as set-point LQG and LQI prior to robust control. In order to see which shape of the sensitivity function is desirable, the different performance indices are defined when designing the LQI. After implementation and analysis of the baseline controllers, a non-conventional sensitivity weighting function is devised that has different slopes in the low frequency and around crossover frequency, which results in improvement of the performance without loss of robustness. This result cannot be accomplished using typical weighting functions such as low-pass filter types.

## 1.4 Thesis organization

---

The study logic of this dissertation is shown in Fig. 1.3. Chapter 2 states the six-degree-of-freedom equations of motion of a launch vehicle. In chapter 3, optimal trajectory generation via virtual motion camouflage (VMC) is described. First, the virtual motion camouflage (VMC) method is introduced in 3.1. VMC is applied to a trajectory generation problem for a launch vehicle in 3.2. Here, a sequential VMC method to adjust nonlinear constraints is also described. Chapter 4 proposes a robust control for the unstable and flexible launch vehicle. First, the model of the launch vehicle and its properties are discussed in 4.1. In 4.2, baseline controllers are designed prior to robust controller. Here, set-point LQG and LQG with integral control are designed, which have a two-degree-of-freedom control

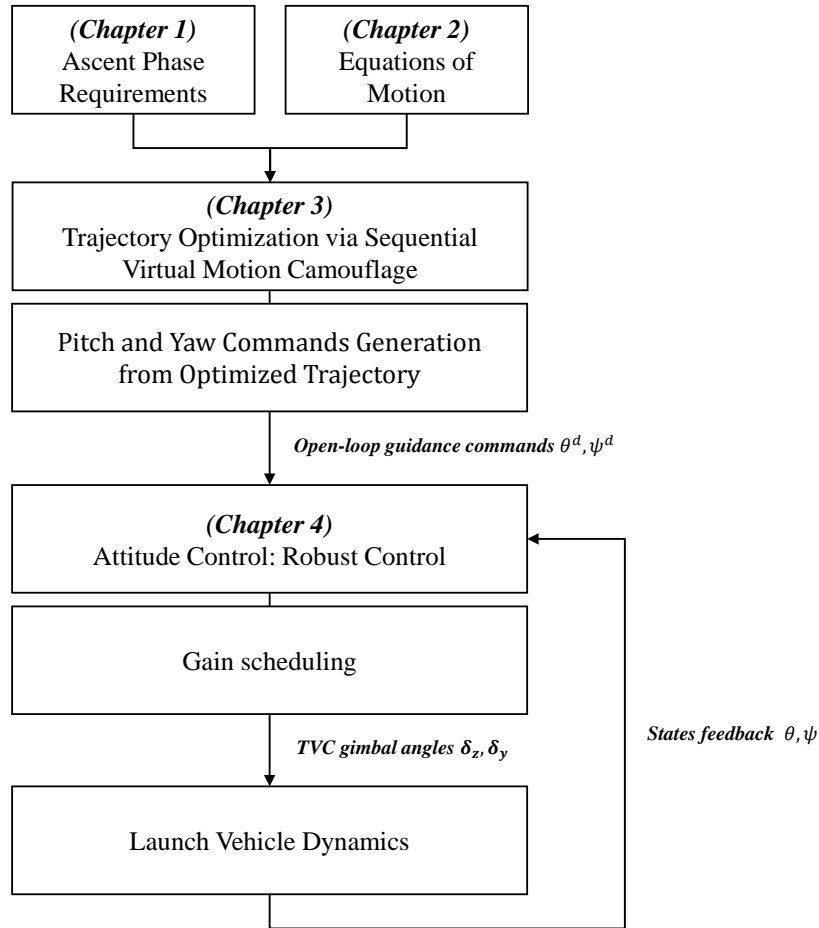


Figure 1.3: Study logic

structure. Chapter 4.3 presents in detail the robust controller designed with a two-degree-of-freedom  $H_\infty$  control. Here, how the weight functions can be designed for improving tracking performance while maintaining robust stability will be explained. In Chapter 4.4, 6-DOF simulation integrated with VMC guidance and robust control is conducted. Chapter 5 summarizes the issues considered in this dissertation provides concluding remarks.

# 2

## Launch Vehicle Dynamics

This section describes a complete set of dynamic models of a launch vehicle incorporating rigid body motion, aerodynamics, thrust and structural flexibility.

### 2.1 Frame and coordinate

---

In this study, two frames and coordinate systems are used. The guidance coordinate system is defined on inertia frame denoted as (I). The origin of the guidance coordinate system is located at the launch site, its  $X$  and  $Z$  axes respectively point the normal to the surface and launch heading, and the  $Y$ -axis completes the right-handed coordinate system. The body-fixed coordinate system is defined on body frame denoted as (b) which is moving with the launch vehicle body. The above frame and coordinate system are illustrated in Fig 2.1

### 2.2 Rigid body motion

---

The six-degree-of-freedom (6-DOF) equations of motion of a launch vehicle consist of the translational motion and rotational motion. The translational equation of motion of the



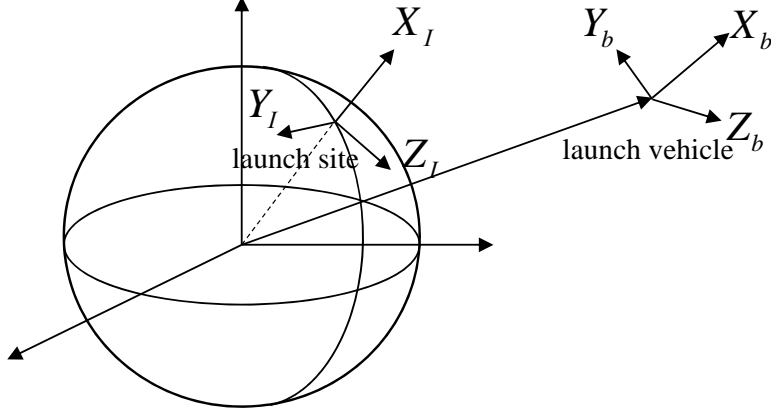


Figure 2.1: Coordinate systems

center of gravity of a launch vehicle is expressed in a inertia frame as follows:

$$\begin{pmatrix} \ddot{X} \\ \ddot{Y} \\ \ddot{Z} \end{pmatrix} = \frac{1}{m} \begin{pmatrix} F_x^I \\ F_y^I \\ F_z^I \end{pmatrix} \quad (2.1)$$

or can be expressed in a body frame

$$\begin{pmatrix} \dot{u} \\ \dot{v} \\ \dot{w} \end{pmatrix} = \frac{1}{m} \begin{pmatrix} F_x^b \\ F_y^b \\ F_z^b \end{pmatrix} - \begin{pmatrix} p \\ q \\ r \end{pmatrix} \times \begin{pmatrix} u \\ v \\ w \end{pmatrix} \quad (2.2)$$

where  $\begin{bmatrix} X & T & Z \end{bmatrix}^T$  is the position vector of a launch vehicle expressed in the guidance coordinate system.  $\begin{bmatrix} u & v & w \end{bmatrix}^T$  and  $\begin{bmatrix} p & q & r \end{bmatrix}^T$  are the vehicle's translational and angular velocities in body frame, respectively.  $F^I = \begin{bmatrix} F_x^I & F_y^I & F_z^I \end{bmatrix}^T$  is the total force acting on the vehicle.

The total inertia force  $F^I$  and body frame force  $F^b$  has the following relationship:

$$F^I = C_{I/b} F^b \quad (2.3)$$

where direction cosine matrix is defined as

$$C_{b/I} = \begin{pmatrix} \cos \theta \cos \psi & \cos \theta \sin \psi & -\sin \theta \\ \sin \phi \sin \theta \cos \psi - \cos \phi \sin \psi & \sin \phi \sin \theta \sin \psi + \cos \phi \cos \psi & \sin \phi \cos \theta \\ \cos \phi \sin \theta \cos \psi + \sin \phi \sin \psi & \cos \phi \sin \theta \sin \psi - \sin \phi \cos \psi & \cos \phi \cos \theta \end{pmatrix}$$

The total force consists of the following three terms

$$F^I = F_{aero}^I + F_{thrust}^I + F_g^I \quad (2.4)$$

where  $F_{aero}^I$ ,  $F_{thrust}^I$  and  $F_g^I$  are the aerodynamic force, the thrust force and gravity force, respectively.

The rotational equation of motion is expressed in a body fixed frame as

$$\begin{pmatrix} \dot{p} \\ \dot{q} \\ \dot{r} \end{pmatrix} = J^{-1} \left[ - \begin{pmatrix} p \\ q \\ r \end{pmatrix} \times J \begin{pmatrix} p \\ q \\ r \end{pmatrix} + T^b \right] \quad (2.5)$$

where  $J = \text{diag} [I_{xx}, I_{yy}, I_{zz}]$  is the inertia matrix of the vehicle and  $T^b$  is the total moment acting on the vehicle. The total moment consists of the following two terms

$$T^b = T_{aero}^b + T_{thrust}^b \quad (2.6)$$

where  $T_{aero}^b$  and  $T_{thrust}^b$  are the aerodynamic moment, the thrust moment, respectively.

The Euler angles are updated by following kinematic equation

$$\begin{pmatrix} \dot{\phi} \\ \dot{\theta} \\ \dot{\psi} \end{pmatrix} = \frac{1}{\cos \theta} \begin{pmatrix} \cos \theta & \sin \psi \sin \theta & \cos \phi \sin \theta \\ 0 & \cos \phi \cos \theta & -\sin \phi \cos \theta \\ 0 & \sin \phi & \cos \phi \end{pmatrix} \begin{pmatrix} p \\ q \\ r \end{pmatrix} \quad (2.7)$$

## 2.3 Aerodynamic forces and moments

---

The aerodynamic forces and moments depend on the air speed. The vehicle's relative velocity vector can be expressed as

$$V_{rel}^I = V^I - V_{wind}^I \quad (2.8)$$

$$V_{rel}^b = C_{b/I} V_{rel}^I \quad (2.9)$$

where,  $V^I$  and  $V_{wind}^I$  are vehicle's velocity and local wind's velocity expressed in the inertia frame. Then the angle of attack, sideslip angle, Mach number and dynamic pressure can be defined using the relative vehicle's velocity.

$$\alpha = \tan^{-1} \left( \frac{V_{rel,x}^b}{V_{rel,z}^b} \right) \quad (2.10)$$

$$\beta = \sin^{-1} \left( \frac{V_{rel,y}^b}{\|V_{rel}^b\|} \right) \quad (2.11)$$

$$M = \frac{\|V_{rel}^b\|}{a} \quad (2.12)$$

$$Q = \frac{1}{2} \rho \|V_{rel}^b\|^2 \quad (2.13)$$

where  $a$  is the speed of sound and  $\rho$  is the air density and they are functions of altitude.

The aerodynamic forces are expressed in the body frame as

$$\begin{aligned}
 D &= QSC_D(M) \\
 Y &= QSC_{Y_\beta}(M)\beta \\
 N &= QSC_{N_\alpha}(M)\alpha
 \end{aligned} \tag{2.14}$$

where  $C_{Y_\beta}(M)$  and  $C_{N_\alpha}(M)$  are the aerodynamic coefficients in  $y$  and  $z$  axes of the body frame and  $C_D(M)$  is the drag coefficient.  $Q$  and  $S$  are dynamic pressure and reference area, respectively.

Then, the aerodynamic forces acting on the vehicle are

$$\begin{aligned}
 F_{aero,x}^b &= -D \\
 F_{aero,y}^b &= C \\
 F_{aero,z}^b &= -N
 \end{aligned} \tag{2.15}$$

and the aerodynamic moments about the center of gravity are

$$\begin{aligned}
 T_{aero,x}^b &= 0 \\
 T_{aero,y}^b &= l_{cp}Y \\
 T_{aero,z}^b &= l_{cp}N
 \end{aligned} \tag{2.16}$$

where  $l_{cp}$  is the length between the center of pressure and the center of mass.

## 2.4 Gravity force

---

The gravity force  $F_g^I$  is defined as

$$F_g^I = m \begin{bmatrix} g_x^I \\ g_y^I \\ g_z^I \end{bmatrix} \quad (2.17)$$

The mass  $m$  is updated by assuming that rocket nozzle is perfectly expanded as

$$\dot{m} = -\frac{T_{vac}}{g_0 I_{sp}} \quad (2.18)$$

where  $T_{vac}$ ,  $g_0$  and  $I_{sp}$  are the thrust force in a vacuum, the acceleration of the gravity and specific impulse measured in seconds.

## 2.5 Thrust forces and moments

---

The thrust is simply modeled as

$$T = T_{vac} - A_e \cdot p_e$$

where  $T$  is the total thrust force.  $T_{vac}$ ,  $A_e$  and  $p_e$  are the total vacuum thrust, the exit area and exit pressure of the nozzle.

Then the components of the thrust force expressed in the body frame are

$$\begin{aligned} F_{thrust,x}^b &= T \\ F_{thrust,y}^b &= -T \delta_z \\ F_{thrust,z}^b &= -T \delta_y \end{aligned} \quad (2.19)$$

where  $\delta_y$  and  $\delta_z$  are the pitch and yaw gimbal deflection angles of TVC, respectively.

The components of the moment generated by the thrust are

$$\begin{aligned}
 T_{aero,x}^b &= 0 \\
 T_{aero,y}^b &= l_{cg}\delta_y \\
 T_{aero,z}^b &= l_{cg}\delta_z
 \end{aligned} \tag{2.20}$$

where  $l_{cg}$  is the length between the center of mass and the gimbal attach point.

## 2.6 Flexible bending modes

---

A flexible bending mode of the vehicle can be modeled as second-order system:

$$\ddot{\eta} + 2\zeta\omega\dot{\eta} + \omega^2\eta = \Phi^T F_{thrust}^b \tag{2.21}$$

where  $\Phi$  is the flex-mode influence matrix at the gimbal attach point.

The effect of bending modes can be modeled by adding perturbation angle at the Euler angles.

$$\begin{pmatrix} \phi_m \\ \theta_m \\ \psi_m \end{pmatrix} = \begin{pmatrix} \phi \\ \theta \\ \psi \end{pmatrix} + \Psi\eta \tag{2.22}$$

where  $\phi_m, \theta_m, \psi_m$  are the sensor measurements of Euler angles and  $\Psi$  is the flex-mode influence matrix at the instrument unit location.

# 3

## Optimal Trajectory Generation

An important issue of a launch vehicle flight is the generating optimal trajectory during its atmospheric ascent while satisfying constraints such as bending moment. These constraints are significantly influenced by wind disturbance, especially in the maximum dynamic pressure region. Generally, atmospheric ascent guidance is conducted as open loop due to the difficulty of finding an analytic solution or real-time optimal guidance in the presence of aerodynamic forces and winds. In this phase, aerodynamic load management is essential because high dynamics pressure region can cause a structural failure from the excessive bending moment. Therefore, an objective of the trajectory generation is the minimization of the aerodynamic load while satisfying designated position and velocity at the final time.

### **3.1 VMC based trajectory optimization**

---

In order to consider dynamics of the launch vehicle, nonlinear constraints are included in a trajectory optimization problem. In this section, general problem formulation of the nonlinear constrained optimization is described followed by the problem formulation using virtual motion camouflage.

### 3.1.1 Nonlinear constrained trajectory optimization problem

The performance index for the typical trajectory optimization is given as

$$J = \varphi [\mathbf{x}(t_f, t_f)] + \int_{t_0}^{t_f} L(\mathbf{x}, \mathbf{u}, t) dt \quad (3.1)$$

subject to the inequality constraints

$$\mathbf{g}(\mathbf{x}, \mathbf{u}, t) \leq 0, \quad \mathbf{g} \in \mathbb{R}^{p \times 1} \quad (3.2)$$

and the equality constraints

$$\mathbf{h}(\mathbf{x}, \mathbf{u}, t) = 0, \quad \mathbf{h} \in \mathbb{R}^{q \times 1}. \quad (3.3)$$

Here,  $\mathbf{x} \in \mathbb{R}^{n \times 1}$ ,  $\mathbf{u} \in \mathbb{R}^{m \times 1}$  and  $t_f$  denote the state vector, control vector and final time, respectively. The equality constraints (3.3) include the following boundary conditions

$$\boldsymbol{\psi} [\mathbf{x}(t_0), \mathbf{x}(t_f), t_0, t_f] = 0, \quad \boldsymbol{\psi} \in \mathbb{R}^{l \times 1} \quad (3.4)$$

and the equations of motion

$$\dot{\mathbf{x}} = f(\mathbf{x}, \mathbf{u}, t). \quad (3.5)$$

The optimal trajectory will be found to minimize (or maximize) the performance index (3.1) in what is called the “full space”. The solution might be locally or globally optimal depending on optimization methods.

### 3.1.2 VMC formulation

In [15, 16], the idea of “motion camouflage” (MC) strategy [14] is applied to the nonlinear constrained trajectory optimization problem, which is called virtual motion camouflage (VMC). The VMC formulation consists of the aggressor  $\mathbf{x}_a(t)$ , virtual prey  $\mathbf{x}_p(t)$  and ref-



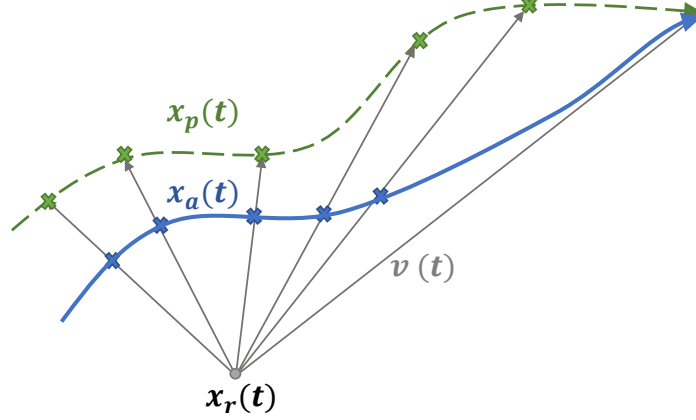


Figure 3.1: VMC concept

reference point  $\mathbf{x}_r(t)$  as shown in Fig. 3.1. The aggressor's path depends on the prey motion and reference point, and can be controlled by the path control parameter (PCP)  $v(t)$  as follows:

$$\mathbf{x}_a = \mathbf{x}_r + v(\mathbf{x}_p - \mathbf{x}_r). \quad (3.6)$$

The derivatives of  $\mathbf{x}_a(t)$  can be obtained as follows:

$$\dot{\mathbf{x}}_a = \dot{\mathbf{x}}_r + \dot{v}(\mathbf{x}_p - \mathbf{x}_r) + v(\dot{\mathbf{x}}_p - \dot{\mathbf{x}}_r) \quad (3.7)$$

$$\ddot{\mathbf{x}}_a = \ddot{\mathbf{x}}_r + \ddot{v}(\mathbf{x}_p - \mathbf{x}_r) + 2\dot{v}(\dot{\mathbf{x}}_p - \dot{\mathbf{x}}_r) + v(\ddot{\mathbf{x}}_p - \ddot{\mathbf{x}}_r). \quad (3.8)$$

The VMC formulation considers the following basic assumptions made in [16].

**Assumption 1.** *The state vector  $\mathbf{x} \in \mathbb{R}^{n \times 1}$  can be rearranged into two parts: the position state  $\mathbf{x}_a(t) \in \mathbb{R}^{n_a \times 1}$  and the state rate  $\mathbf{x}_{sr}(t) \in \mathbb{R}^{(n-n_a) \times 1}$ . Correspondingly, the equations of motion  $\dot{\mathbf{x}} = f(\mathbf{x}, \mathbf{u}, t)$  can be rewritten into two parts:  $\dot{\mathbf{x}}_a = f_a(\mathbf{x}, t)$  and  $\dot{\mathbf{x}}_{sr} = f_{sr}(\mathbf{x}, \mathbf{u}, t)$ .*

**Assumption 2.** *The mappings from  $(\mathbf{x}_a, \dot{\mathbf{x}}_a, t)$  to  $\mathbf{x}_{sr}$  and from  $(\mathbf{x}, \dot{\mathbf{x}}, t)$  to  $\mathbf{u}(t)$  are assumed to be injective, which means the control variables  $\mathbf{u}(t)$  and the state rate  $\mathbf{x}_{sr}(t)$  can be solved by  $\mathbf{x}_{sr} = f_a^{-1}(\mathbf{x}_a, \dot{\mathbf{x}}_a, t)$  and  $\mathbf{u} = f_{sr}^{-1}(\mathbf{x}, \dot{\mathbf{x}}_{sr}, t)$  either explicitly or implicitly using an iterative fashion.*

Based on Assumptions 1, 2 and Eqs. (3.6)-(3.8), the state and control variables can be represented as functions of the PCP, prey motion, reference point, and their corresponding derivatives. Therefore, given  $\mathbf{x}_r(t)$  and  $\mathbf{x}_p(t)$ , the original optimization problem represented in Section 3.1.1 can be transformed as follows:

$$J = \varphi[v, \dot{v}, \ddot{v}, \dots, t_f] + \int_{t_0}^{t_f} L(v, \dot{v}, \ddot{v}, \dots, t) dt \quad (3.9)$$

subject to the state and control inequality constraints

$$\mathbf{g}(v, \dot{v}, \ddot{v}, \dots, t_f) \leq 0, \quad \mathbf{g} \in \mathbb{R}^{p \times 1} \quad (3.10)$$

and the equality constraints

$$\mathbf{h} = \psi(v, \dot{v}, \ddot{v}, \dots, t_0, t_f) = 0, \quad \boldsymbol{\psi} \in \mathbb{R}^{l \times 1}. \quad (3.11)$$

Here, the boundary conditions are only considered as the equality constraints since the system dynamics (3.5) are already involved when calculating  $\mathbf{x}_{sr}(t)$  and  $\mathbf{u}(t)$  based on Assumption 2.

In order to obtain the numerical solution through nonlinear programming, the PCP  $v(t)$  is discretized into the PCP nodes  $v_k$ ,  $k = 0, \dots, N$  using Legendre-Gauss-Lobatto (LGL) pseudospectral method. The vector form of the discretized PCP nodes is denoted by  $\mathbf{v} = [v_0, \dots, v_N]^T$  where  $v_0 = v(t_0)$  and  $v_N = v(t_f)$ . The PCP time history is approximated using the Lagrange interpolation polynomials [38] as

$$\mathbf{v}(\tau) \approx \sum_{i=0}^N v_i \beta_i(\tau) \quad (3.12)$$

where the base functions  $\beta_i(\tau)$ ,  $i = 1, \dots, N$ , are the Lagrange interpolating polynomials of order  $N$ . The scaled time  $\tau$  is zeros of  $\dot{L}_N$  which is the derivative of the Legendre polynomial

$L_N$ , and is defined as follows:

$$\tau = \frac{2t - t_f - t_0}{t_f - t_0} \in [-1, 1]. \quad (3.13)$$

In the original time scale  $t$ , the  $k$ -th time derivatives of the PCP vector is obtained as

$$\frac{d^k \mathbf{v}}{dt^k} = \left[ \frac{2}{t_f - t_0} \right]^k \mathbf{D}^k \mathbf{v} \quad (3.14)$$

where the differentiation matrix  $\mathbf{D}$  can be found in [38].

As a consequence, the performance index (3.9) can be rewritten as the following discretized form:

$$J = \varphi[\mathbf{v}, t_f] + \frac{t_f - t_0}{2} \sum_{k=0}^N L(\mathbf{v}) w_k \quad (3.15)$$

where  $w_k$  is the weights for the  $k$ -th LGL node. The inequality and equality constraints can be formed as

$$\mathbf{g}(\mathbf{v}, t_f) \leq 0 \quad (3.16)$$

$$\mathbf{h}(\mathbf{v}, t_f) = 0. \quad (3.17)$$

The solution space is contained by selected  $\mathbf{x}_r$  and  $\mathbf{x}_p$ . Then trajectory is controlled by PCP nodes  $\mathbf{v}$  in given  $\mathbf{x}_r$  and  $\mathbf{x}_p$ . Therefore, selection of the reference point and prey motion is very important and how to select these will be discussed in Section 3.2.2. With selected reference point and prey motion, the optimal trajectory can be obtained by solving the parameter optimization problem with respect to the PCP nodes. In this way, the problem size is reduced from  $3N$  to  $N$  in the 3-D trajectory optimization problem.

## 3.2 VMC based trajectory optimization applied to the launch vehicle

---

In this section, VMC based trajectory optimization method is applied to the launch vehicle during ascent phase. First, how guidance inputs are generated from the optimized path will be explained. Next, the optimal trajectory generation problem is formulated using the VMC framework described in the previous section.

### 3.2.1 Relationship between launch vehicle dynamics and VMC

By summing that the axial force ( $f_x$ ) is dominant relative to other axes ( $f_y, f_z$ ), and TVC angles are small, the 3-DOF translational equation of motion can be expressed as

$$\begin{pmatrix} \ddot{X} \\ \ddot{Y} \\ \ddot{Z} \end{pmatrix} = \frac{1}{m} \begin{pmatrix} f_x \cos \theta \cos \psi - mg \\ f_x \cos \theta \sin \psi \\ f_x \sin \theta \end{pmatrix} \quad (3.18)$$

where axial force  $f_x = T - D$  and  $(X, Y, Z)$  denotes the inertial position of the vehicle.

For the VMC formulation, the state vector is defined as  $\mathbf{x} = [X \ Y \ Z \ \dot{X} \ \dot{Y} \ \dot{Z}]^T$ . Based on Assumption 1, the state vector is separated into two parts: the position state vector  $\mathbf{x}_a = [X \ T \ Z]^T$ , and the state rates vector  $\mathbf{x}_{sr} = [\dot{X} \ \dot{Y} \ \dot{Z}]^T$ . Using (3.6)-(3.8), the position state of the aggressor and its derivatives are given as

$$\mathbf{x}_a = \mathbf{x}_r + v(\mathbf{x}_p - \mathbf{x}_r) \quad (3.19)$$

$$\dot{\mathbf{x}}_a = \dot{v}(\mathbf{x}_p - \mathbf{x}_r) + v\dot{\mathbf{x}}_p \quad (3.20)$$

$$\ddot{\mathbf{x}}_a = \ddot{v}(\mathbf{x}_p - \mathbf{x}_r) + 2\dot{v}\dot{\mathbf{x}}_p + v\ddot{\mathbf{x}}_p \quad (3.21)$$

where  $\mathbf{x}_r$  remains fixed in this study during optimization. The selection of the prey motion  $\mathbf{x}_p$  and the reference point  $\mathbf{x}_r$  will be discussed in Section 3.2.2.

The guidance inputs of the launch vehicle are desired Euler angles for pitch plane  $\theta$  and yaw plane  $\psi$ . Using the dynamic equation (3.18), the guidance inputs can be calculated as

$$\theta = \sin^{-1} \left( \frac{m\ddot{Z}}{-f_x} \right) \quad (3.22)$$

$$\psi = \tan^{-1} \left( \frac{\ddot{Y}}{\ddot{X} + g} \right) . \quad (3.23)$$

In this study, the thrust is predetermined regardless of trajectory. Therefore, the constraint on the total velocity has to be considered in the optimization. The derivative of the total speed with given scheduled thrust can be calculated as

$$\dot{V}^d = \frac{f_x \cos \alpha \cos \beta + f_y \sin \beta + f_z \sin \alpha \cos \beta}{m} - g \cos \gamma \cos \chi \quad (3.24)$$

where the flight path angle  $\gamma$ , heading angle  $\chi$  and the derivative of the total velocity  $V$  can be calculated as

$$\gamma = \sin^{-1} \left( \frac{\dot{Z}}{\dot{V}} \right) \quad (3.25)$$

$$\chi = \tan^{-1} \left( \frac{\dot{Y}}{\dot{X}} \right) \quad (3.26)$$

$$\dot{V} = \frac{\dot{\mathbf{x}}_a^T \ddot{\mathbf{x}}_a}{V} . \quad (3.27)$$

The aerodynamic angles such as the angle of attack  $\alpha = \tan^{-1}(w/u)$  and the sideslip angle  $\beta = \sin^{-1}(v/V)$  can be calculated from the definition as

$$\alpha = \tan^{-1} \left( \frac{\tan \theta \cos (\psi - \chi) + \tan \gamma}{\cos (\psi - \chi) - \tan \theta \tan \gamma} \right) \quad (3.28)$$

$$\beta = \sin^{-1} (\cos \gamma \sin (\chi - \psi)) . \quad (3.29)$$

### 3.2.2 Selection of reference point and virtual prey motion

The selection of the virtual prey motion and reference point is important because it is closely related to the problem space. They can be selected to reflect physical meaning and making a reasonable initial guess is not difficult.

In the planar motion, the appropriate reference point can be selected on the line which is perpendicular to the center point of the prey motion [17]. Whereas, in 3-D space, the selection of the reference point can be a convoluted problem. In [16], the sequential VMC method involving two steps in an iteration process is proposed to solve this problem. In the first step, an optimal solution can be found within subspace constructed by reference point, and then a linear programming and a line search algorithm are used in the second step to improve reference point.

In this study, the reference point is placed on the line which is tangential to the direction of the initial vehicle's velocity as follows

$$\mathbf{x}_r = \mathbf{x}_{a,0} + k\dot{\mathbf{x}}_{a,0} \quad (3.30)$$

where  $k$  is a scale factor.  $\mathbf{x}_{a,0}$  and  $\dot{\mathbf{x}}_{a,0}$  denote the initial position and velocity vector of the aggressor, respectively. At the end of the ascent phase, the final position and velocity have to be satisfied at preplanned time. Therefore, the vehicle has the initial and terminal boundary conditions  $\mathbf{x}_{a,0}$ ,  $\dot{\mathbf{x}}_{a,0}$ ,  $\mathbf{x}_{a,f}$  and  $\dot{\mathbf{x}}_{a,f}$ . Since there exist twelve boundary conditions in 3-D, the virtual prey motion can be selected as the following polynomials:

$$\mathbf{x}_p = \begin{bmatrix} x_{p,x} \\ x_{p,y} \\ x_{p,z} \end{bmatrix} = \begin{bmatrix} a_1 t^3 + b_1 t^2 + c_1 t + d_1 \\ a_2 t^3 + b_2 t^2 + c_2 t + d_2 \\ a_3 t^3 + b_3 t^2 + c_3 t + d_3 \end{bmatrix}. \quad (3.31)$$

The coefficients  $a_i$ ,  $b_i$ ,  $c_i$ , and  $d_i$ ,  $i = 1, 2, 3$  are determined by the initial and final boundary conditions. From (3.31), we can obtain the prey motion satisfying the initial and final

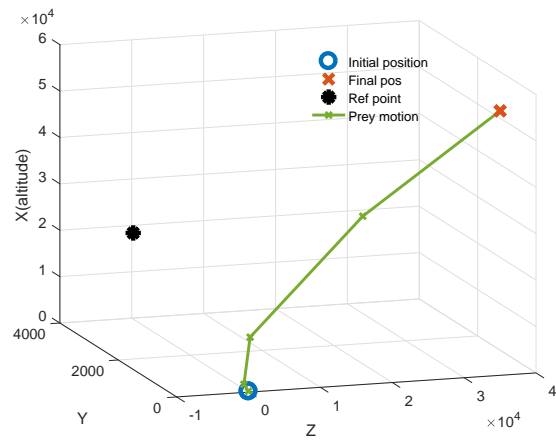


Figure 3.2: Reference point and prey motion

position and orientation of the launch vehicle. The designed reference point and prey motion are represented in Fig. 3.2

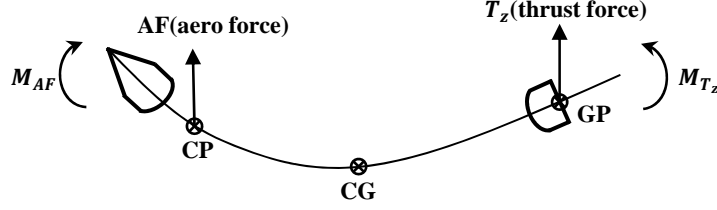


Figure 3.3: Aerodynamic load

### 3.2.3 Trajectory optimization via VMC

In this subsection, VMC is applied to a trajectory optimization problem for the launch vehicle during ascent phase. An ascent flight trajectory can be separated into vertical flight and transition turn. After lift-off, the launch vehicle flies vertically and turns slowly toward the designed position by using TVC (thrust vector control). A trajectory optimization is conducted after the vertical flight.

In the transition turn, aerodynamic forces acting on the center of pressure increase as dynamic pressure increases. To maintain the equilibrium of moments, the thrust force from the TVC has to be generated. As a result, the significant bending moment is applied to the launch vehicle as shown in Fig. 3.3, which can cause a structural failure of the vehicle [39]. Therefore, the trajectory optimization problem is formulated to minimize the maximum aerodynamic load while satisfying final conditions of the position and velocity of the vehicle. The aerodynamic load can be defined as  $Q\alpha_T$ . Here,  $Q$  and  $\alpha_T$  are the dynamic pressure and the total angle of attack, respectively.

The nonlinear optimization problem is defined as follows:

Given  $\mathbf{x}_r$  and  $\mathbf{x}_p$ ,  $\mathbf{v} = [v_k]_{k=0,1,\dots,N}$  will be designed to minimize the performance index

$$J = \max_{t \in [t_0, t_f]} (Q(t)\alpha_T(t)) \quad (3.32)$$



subject to

$$\|\dot{V}(t) - \dot{V}^d(t)\| < 1 \quad (3.33)$$

$$\|\theta(t_0)\| < 5^\circ \quad (3.34)$$

$$\|\psi(t_0)\| < 5^\circ \quad (3.35)$$

$$-\pi/2 < \theta(t) < \pi/2 \quad (3.36)$$

$$-\pi/2 < \psi(t) < \pi/2 \quad (3.37)$$

$$x_a(t_0) = P_{CM,0} \quad (3.38)$$

$$V(t_0) = V_{CM,0} \quad (3.39)$$

$$x_a(t_f) = P_{CM,f} \quad (3.40)$$

$$V(t_f) = V_{CM,f} \quad (3.41)$$

where  $P_{CM}$  and  $V_{CM}$  are the position vector and the velocity vector of the launch vehicle. Each constraint is included for the following reasons:

Since thrust force of the vehicle is preplanned, the derivative of the velocity is determined regardless of the trajectory. The desired velocity is calculated as in Eq. (3.24). Therefore, the derivative of the velocity constraint Eq. (3.33) is considered. As mentioned before, the launch vehicle flies vertically at the beginning of the ascent phase. For this, the commands are set to  $\theta = 0$  and  $\psi = 0$  during vertical flight. Therefore, to keep the command smooth between vertical flight and transition turn, the constraints Eqs. (3.34) and (3.35) are included. Eqs. (3.36) and (3.37) are to constrain guidance input range. The equality constraints Eqs. (3.38)-(3.41) are included for boundary conditions.

In the above problem formulation, the equality constraints are about the boundary conditions. In the VMC, PCP and prey motion at specific nodes can be calculated rather than optimized or guessed to satisfy the boundary conditions [16]. By calculating them, the equality constraints are not included in optimization. As a result, the optimal trajectory can be obtained by solving the following optimal problem without equality constraints:

Given  $\mathbf{x}_r$  and  $\mathbf{x}_p$ ,  $\mathbf{v} = [v_k]_{k=2,\dots,N-2}$  will be designed to minimize the performance index

$$J = \max_{t \in [t_0, t_f]} (Q(t)\alpha_T(t)) \quad (3.42)$$

subject to

$$\begin{aligned} \|\dot{V}(t) - \dot{V}^d(t)\| &< 1 \\ \|\theta(t_0)\| &< 5^\circ \\ \|\psi(t_0)\| &< 5^\circ \\ -\pi/2 &< \theta(t) < \pi/2 \\ -\pi/2 &< \psi(t) < \pi/2 . \end{aligned} \quad (3.43)$$

It is solved by using sequential quadratic programming (SQP) method.

**Remark 1.** For boundary condition, we set  $v_0 = 1$ ,  $v_N = 1$ ,  $x_{a,0} = x_{p,0}$ ,  $x_{a,N} = x_{p,N}$  which results in  $x_{a,0} = x_0$ ,  $x_{a,f} = x_f$ , and  $v_1, v_{N-1}$  are calculated based on Lemmas 1-3 of [16] to satisfy  $\dot{x}_{a,0} = \dot{x}_0$  and  $\dot{x}_{a,f} = \dot{x}_f$ .

### 3.2.4 Sequential VMC: constraint correction

In the VMC formulation, solution space is limited by the prey motion and the reference point. By the virtue of this subspace search, the computation time can be reduced. However, a problem can arise when the constructed subspace (defined by the selected prey motion and reference point) does not contain a solution which satisfies the constraints. Since the launch vehicle dynamics is usually nonlinear and complicated in 3-D space, this may occur easily.

A way to address this concern is to adjust subspace by updating prey motion and the reference point. In [16], the sequential VMC method is proposed involving two steps. In the first step, an optimal solution can be found within subspace, and then a linear

programming and a line search algorithm are used in the second step to update the reference point for improving cost function. This approach may work well when constraints are already satisfied, and performance enhancement is the only concern. On the other hand, in our problem, we utilize a sequential problem as a “constraint correction” step to find an updating direction that makes subspace contains a feasible solution.

The sequential VMC method is introduced here to adjust the subspace after a solution has been found within the initial subspace. For constraint correction, a quadratic programming (QP) is used to find a correcting direction by neglecting the term related to the cost function. It means that we do not put any restriction to the cost function in the constraint correction step. The QP sub-problem is defined as follows:

Given the subspace solution found at the  $k$ -th VMC optimization, an improving direction  $\mathbf{d}$  can be found by minimizing

$$0.5\mathbf{d}^T \mathbf{d} \tag{3.44}$$

subject to

$$\left. \frac{\partial g_i}{\partial X_s} \right|_k d_k \leq -g_i|_k, \quad i = 1, \dots, p \tag{3.45}$$

and

$$-\Delta_{jl} \leq d_j \leq \Delta_{ju}, \quad j = 1, \dots, n_s \tag{3.46}$$

where,  $g_i$  are the inequality constraints and the variable  $X_s \in R^{n_s}$  includes the variables about the discretized  $\mathbf{v}$ ,  $\mathbf{x}_p$  and  $\mathbf{x}_r$  as

$$X_s = [(v_2 \ v_3 \ \dots \ v_N), (x_r \ y_r \ z_r), (x_{p1} \ y_{p1} \ z_{p1}), (x_{p2} \ y_{p2} \ z_{p2}), \dots, (x_{pN} \ y_{pN} \ z_{pN})]^T . \tag{3.47}$$

In the QP problem, constraints are linearized in the current optimization point. Thus

parameters should not change too much to justify the linear approximations. Therefore, move limit  $\Delta_{ji}$  and  $\Delta_{ju}$  are incorporated to limit the magnitude of the updating direction. Here, 30 percent of the current value is defined as the move limit.

After solving the QP, the next subspace is defined as follows

$$X_s^{new} = X_s + d \quad (3.48)$$

where  $\mathbf{v}$  in  $X_s^{new}$  is used as the initial value of the next VMC optimization. The next VMC optimization is conducted with the updated subspace constructed by  $\mathbf{x}_r$  and  $\mathbf{x}_p$  in  $X_s^{new}$ . This sequential VMC is illustrated in Fig. 3.4. Here, the prey motion and the reference point are updated to improve subspace.

The entire sequential VMC algorithm is summarized as below.

step1 : Initial guess for  $\mathbf{x}_p$  and  $\mathbf{x}_r$

step2 : VMC optimization is solved with the given  $\mathbf{x}_p$  and  $\mathbf{x}_r$ .

If the current solution satisfies constraints, algorithm stops. Otherwise, go to Step 3

step3 : QP sub-problem is solved for a constraint correction and updates the subspace.

step4 : VMC optimization is solved with the updated  $\mathbf{x}_p$  and  $\mathbf{x}_r$ .

If the current solution satisfies constraints, algorithm stops. Otherwise, go to Step 3.

### 3.2.5 Comparison study

In order to compare with the optimal result, the conventional direct input programming method and pseudospectral method are examined, which are full-space approaches. For comparison, the same performance index is considered.

First, the direct input programming method in [40] is introduced. The parameter vector

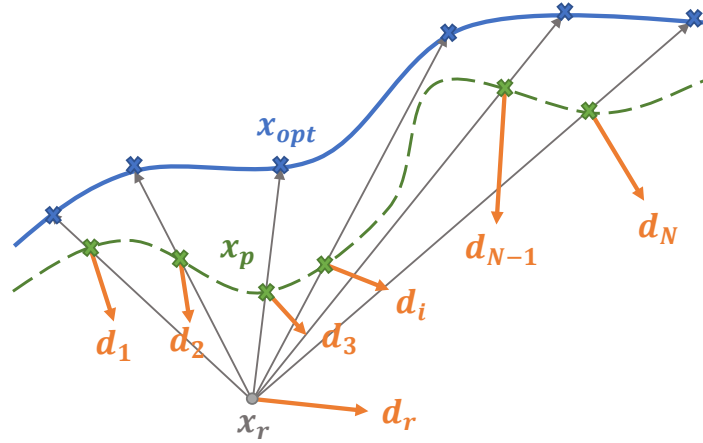


Figure 3.4: Sequential VMC, update of prey motion and reference point by improving direction ‘d’

to be optimized is defined as

$$\mathbf{U}_{DIP} = [\theta(t_1), \theta(t_2), \dots, \theta(t_N), \psi(t_1), \psi(t_2), \dots, \psi(t_N)]^T . \quad (3.49)$$

The nonlinear optimization problem for the load relief is formulated as follows:

The input parameter vector  $\mathbf{U}_{DIP}$  will be designed to minimize the performance index

$$J = \max_{t \in [t_0, t_f]} (Q(t) \alpha_T(t)) \quad (3.50)$$

subject to

$$\begin{aligned} -\pi/2 &< \theta(t) < \pi/2 \\ -\pi/2 &< \psi(t) < \pi/2 \\ x_a(t_0) &= P_{CM,0} \\ V(t_0) &= V_{CM,0} \\ x_a(t_f) &= P_{CM,f} \\ V(t_f) &= V_{CM,f} . \end{aligned} \quad (3.51)$$

The above optimal problem is solved by using sequential quadratic programming (SQP).

Next, the pseudospectral method [11] is performed using the input parameter vector

$$\mathbf{U}_{PSM} = \left[ (X_1, Y_1, Z_1)^T, \dots, (X_N, Y_N, Z_N)^T \right]^T \quad (3.52)$$

where  $(X_i, Y_i, Z_i)^T$  are the inertia position of the vehicle in 3-D dimension and  $N$  is the number of discretized nodes. These discretized nodes are defined as Legendre-Gauss-Lobatto(LGL) points. As a result, the number of optimal parameters is  $3N$ . The nonlinear optimization problem for the load relief is formulated as follows:

The parameter vector  $\mathbf{U}_{PSM}$  will be designed to minimize the performance index

$$J = \max_{t \in [t_0, t_f]} (Q(t) \alpha_T(t)) \quad (3.53)$$

subject to

$$\begin{aligned} -\pi/2 &< \theta(t) < \pi/2 \\ -\pi/2 &< \psi(t) < \pi/2 \\ x_a(t_0) &= P_{CM,0} \\ V(t_0) &= V_{CM,0} \\ x_a(t_f) &= P_{CM,f} \\ V(t_f) &= V_{CM,f} . \end{aligned} \quad (3.54)$$

The above optimal problem is solved by using sequential quadratic programming (SQP).

### 3.3 Numerical simulations

---

In this section, a numerical simulation is conducted to demonstrate the proposed sequential VMC method for trajectory generation. The information of the considered launch vehicle is given in Table. 3.1. The specification of the ascent phase mission is described in Fig. 3.5.

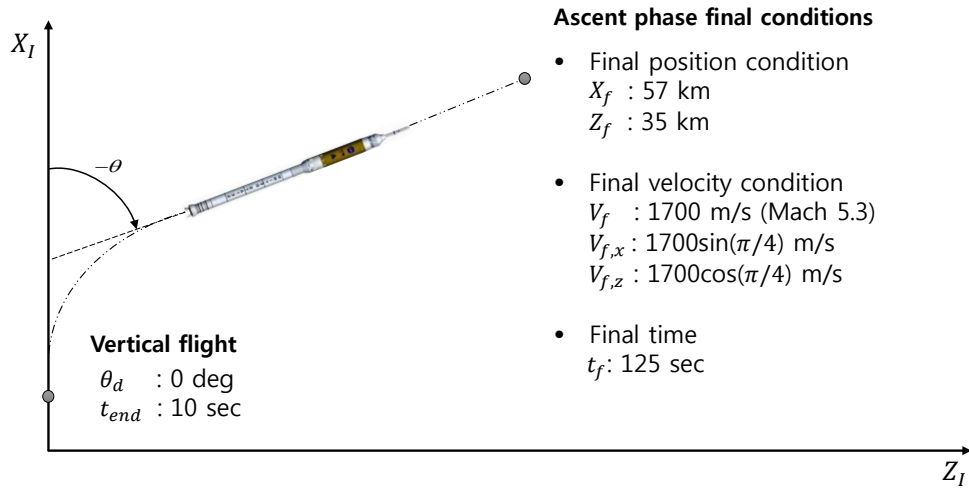


Figure 3.5: Ascent phase mission

Table 3.1: Launch vehicle specifications

Description	Value
Launch mass	200 ton
Launch thrust	3000 kN
Maximum allowed aerodynamic load	2600 Pa rad

Table 3.2 shows the initial and final conditions of the ascent phase.

In the ascent phase flight, the bending moment is significantly influenced by wind disturbance, especially in the maximum dynamic pressure region. The reference wind profile considered in this study is shown in Fig. 3.6. The four cases are considered depending on wind profile as follows:

- case 1: No wind
- case 2: X-axis wind
- case 3: Z-axis wind
- case 4: X, Z-axes wind

Table 3.2: Ascent phase mission

Description	Value
Initial position	$[ 0 \ 0 \ 0 ]$ km
Final position	$[ 57 \ 0 \ 35 ]$ km
Final velocity	$[ 1700 \sin(\pi/4) \ 0 \ 1700 \cos(\pi/4) ]$ m/s
Final time	125 sec

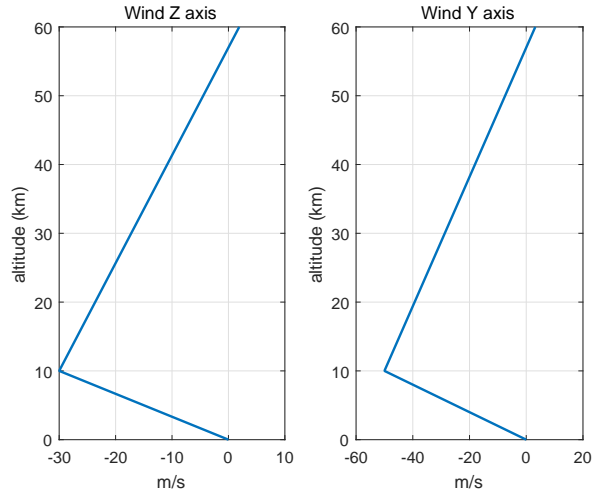


Figure 3.6: Reference wind profile

Since the discretized nodes are placed sparsely in VMC method, the intermediate guidance input is calculated by the interpolation method. In order to check the reliability of the discretized numerical solution, the solution trajectory is reconstructed by numerical integration with forth-order Runge-Kutta denoted as “RK4” and compared with discretized trajectory. The result of reconstruction simulation is shown in Figs. 3.7 and 3.8. From the results, the discretized method is reliable when 20 nodes are used. Therefore, the number of the discretized nodes in the remain simulation is set as 5, 10, 15 and 20 to see its effect.



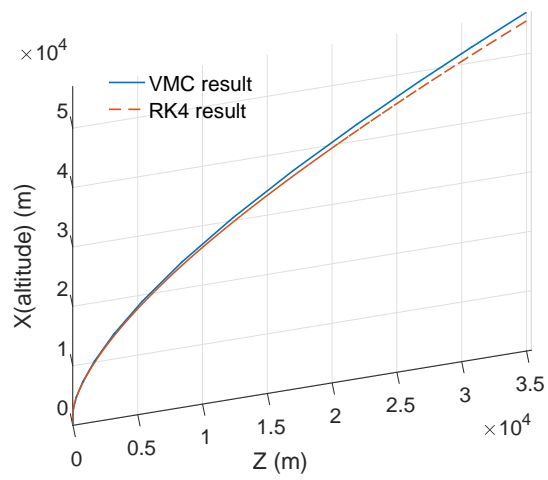
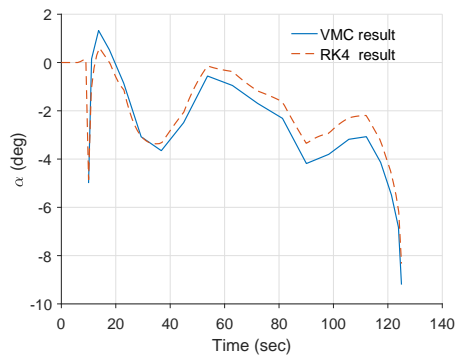
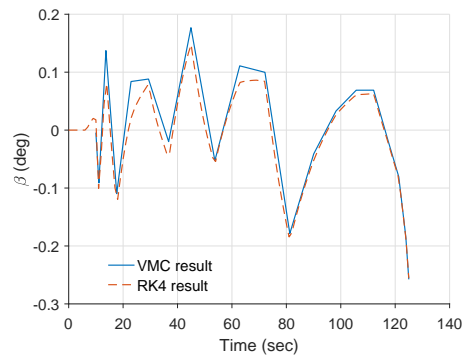


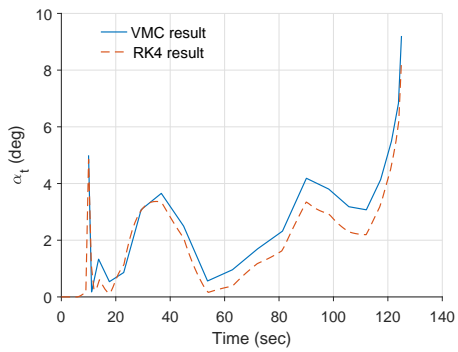
Figure 3.7: Trajectory comparison (RK4 and 20 nodes)



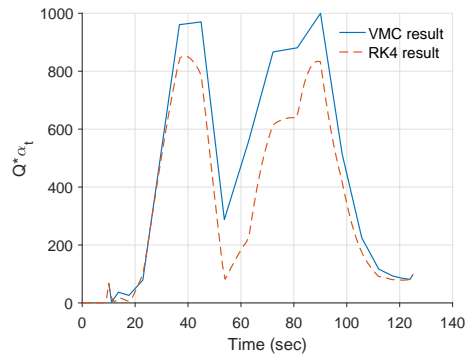
(a) angle of attack



(b) sideslip angle



(c) total angle of attack

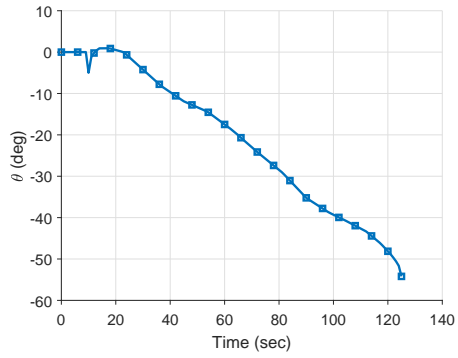


(d) aerodynamic load

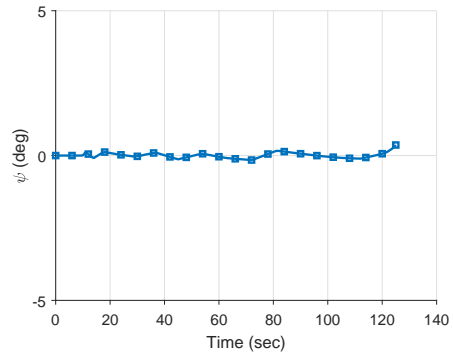
Figure 3.8: Comparison of aerodynamic angles (RK4 and 20 nodes)

### 3.3.1 Case 1: No wind disturbance

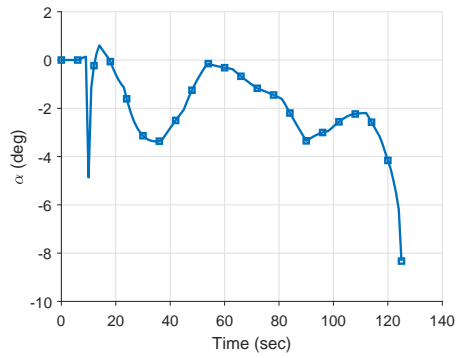
The optimization results with 20 nodes are shown in Fig. 3.9. The pitch command and yaw command inputs are shown in Fig. 3.9(a) and (b). Since the  $Z$ -axis is defined to the direction of the final heading angle, yaw command did not require when there exists no wind disturbance. In Fig. 3.9(c), the angle of attack has the small value from 50 to 70 seconds where the maximum dynamic pressure occurs. The sideslip angle has nearly zero value for the same reason of the yaw command as shown in Fig. 3.9(d). The aerodynamic load is shown in Fig. 3.9(f). The optimized trajectory shown in Fig. 3.10 satisfies all constraints.



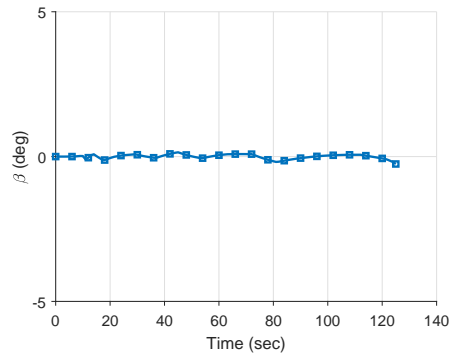
(a) pitch command



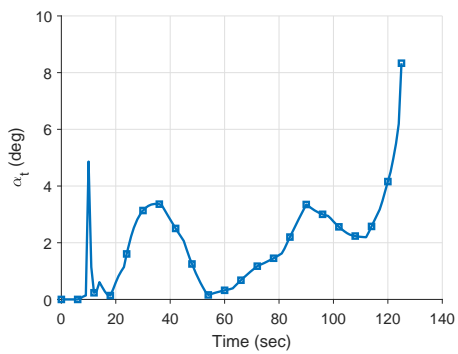
(b) yaw command



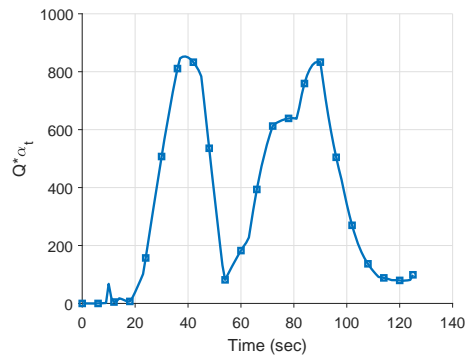
(c) angle of attack



(d) sideslip angle

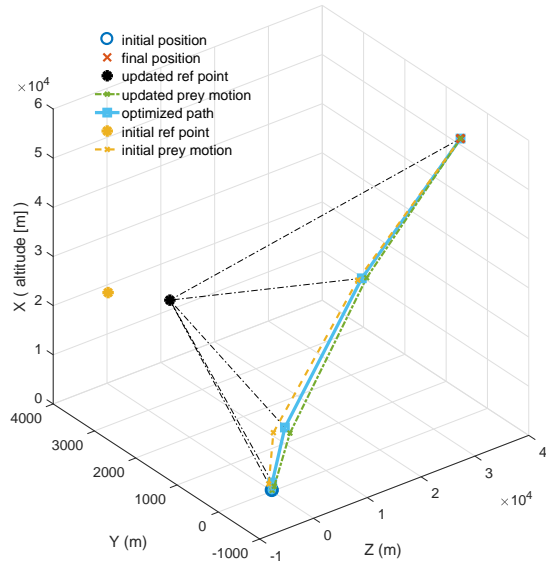


(e) total angle of attack

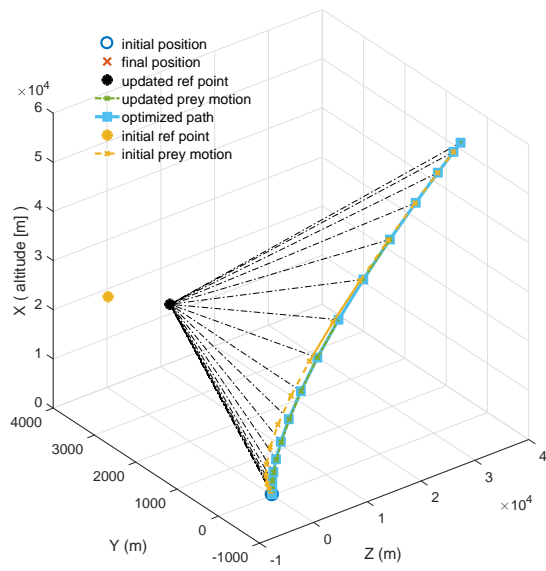


(f) aerodynamic load

Figure 3.9: Optimization results of case 1: No wind (using 20 nodes)



(a) using 5 nodes



(b) using 20 nodes

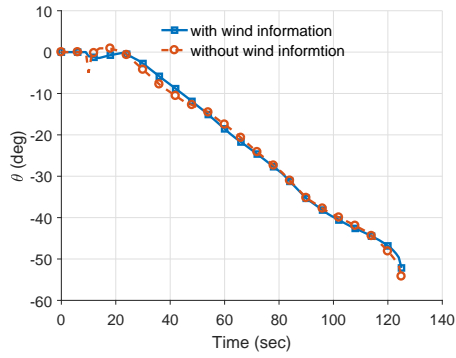
Figure 3.10: Trajectory results of case 1: No wind

### 3.3.2 Case 2: $Z$ -axis wind disturbance

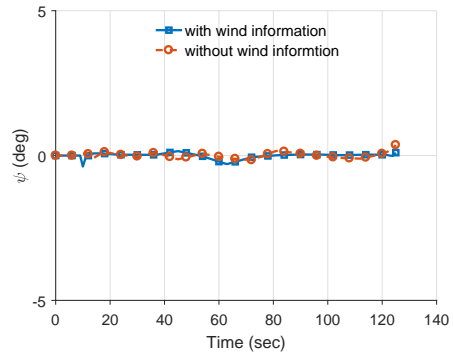
The optimization results using 20 nodes are shown in Fig. 3.11. The results are compared with the result when wind disturbance is not considered. The solid blue lines denote optimization results considering wind disturbance, and the red dashed lines denote results without considering wind disturbance.

The pitch command and yaw command inputs are shown in Figs. 3.11(a) and (b). In Fig. 3.11(c), the angle of attack has small values at 50 to 70 seconds where the maximum dynamic pressure occurs. Since  $Z$ -axis wind is related to the pitch plane, the angle of attack history is quite different from no wind considering case. The sideslip angle has nearly zero value with the same reason of the yaw case as shown in Fig. 3.11(d). In Fig. 3.11(f), the optimized trajectory can reduce aerodynamic load when considering wind, while the aerodynamic load is significantly large when optimization is conducted without wind. The optimized trajectories are shown in Fig. 3.12.

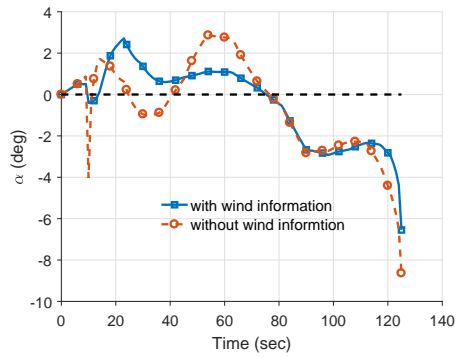
The optimization is conducted with various  $Z$ -axis wind profile to find the tendency of the resulting trajectory. The results are shown in Figs. 3.13 and 3.14. From the trajectory results shown in Fig. 3.13, the influence of the  $Z$ -axis wind to the trajectory is not significant. This tendency is caused by that  $Z$ -axis velocity of the vehicle is very large when compared with other axes velocity and the wind disturbance velocity.



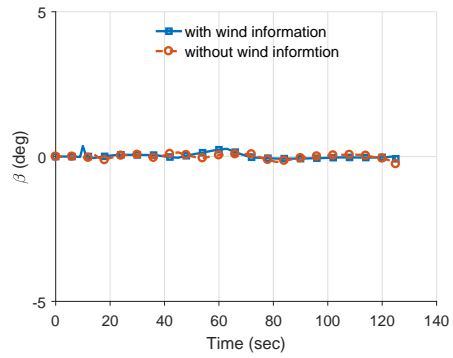
(a) pitch command



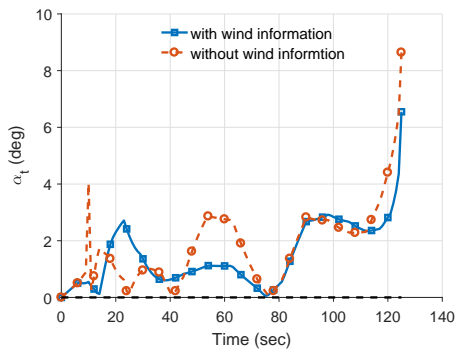
(b) yaw command



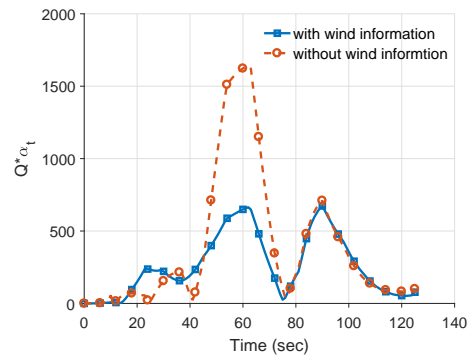
(c) angle of attack



(d) sideslip angle



(e) total angle of attack



(f) aerodynamic load

Figure 3.11: Optimization results of case 2: Z-axis wind (using 20 nodes)

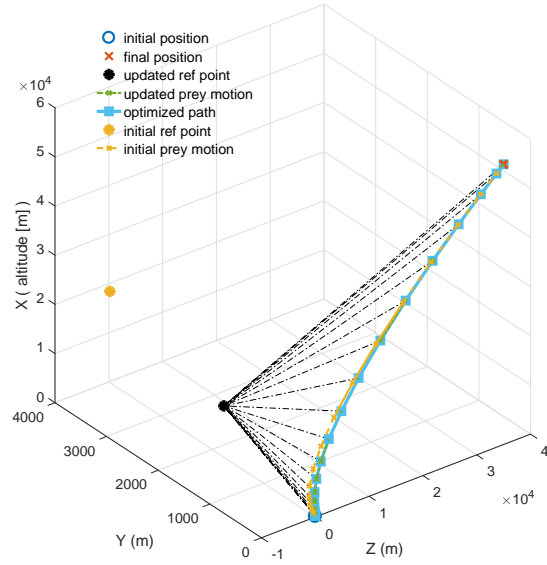
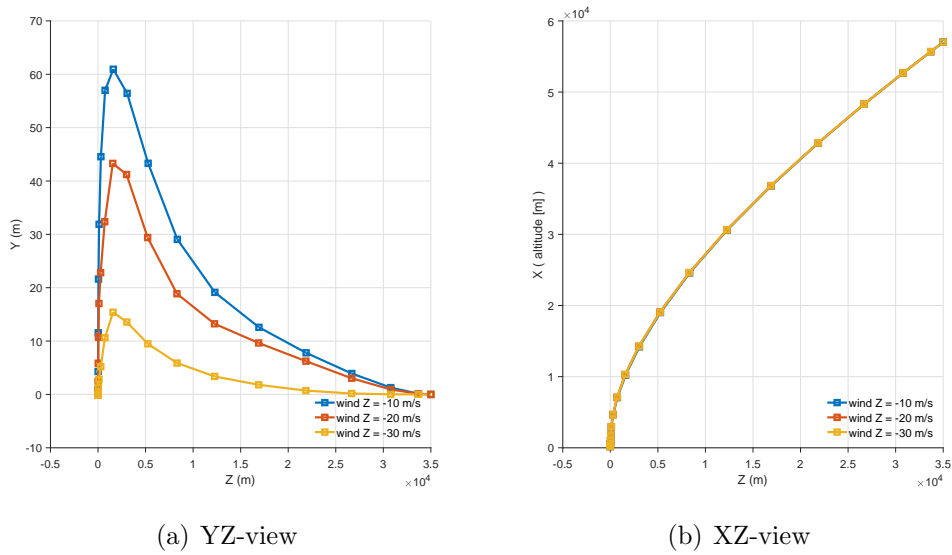


Figure 3.12: Trajectory result of case 2: Z-axis wind (using 20 nodes)

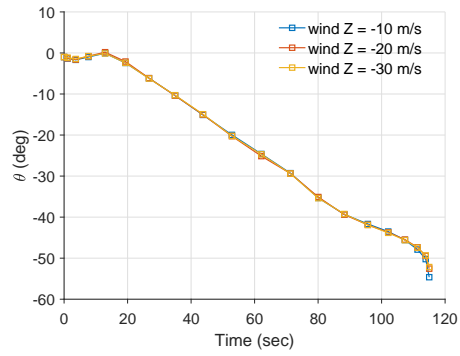


(a) YZ-view

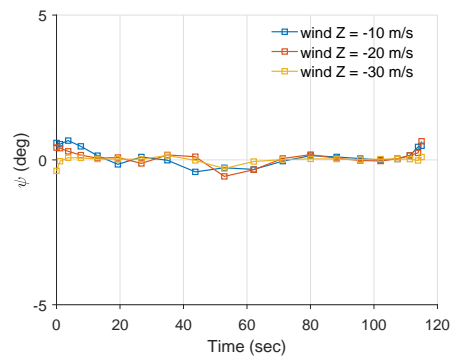
(b) XZ-view

Figure 3.13: Trajectory results of case 2: various Z-axis wind (using 20 nodes)

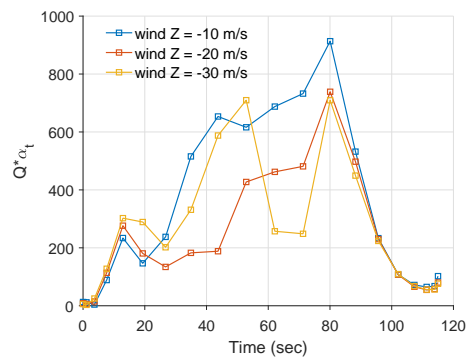




(a) pitch command



(b) yaw command



(c) aerodynamic load

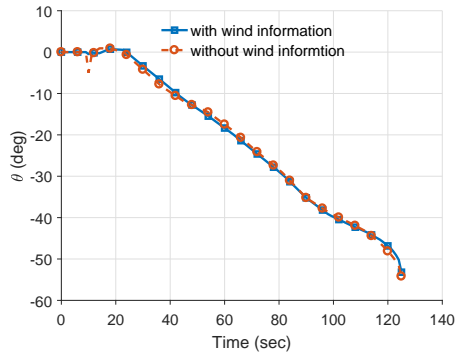
Figure 3.14: Optimization results of case 2: various  $Z$ -axis wind (using 20 nodes)

### 3.3.3 Case 3: $Y$ -axis wind disturbance

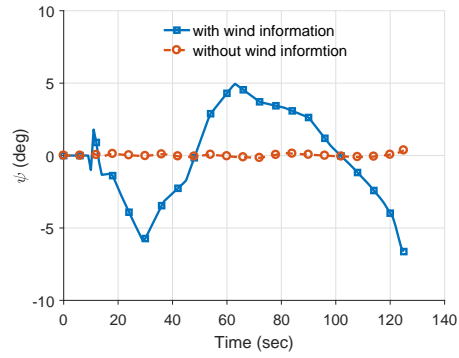
Here, the simulation results with  $Y$ -axis wind disturbance are examined. The optimization result using 20 nodes are shown in Fig. 3.15. The results are compared with the result when wind disturbance is not considered.

The pitch command and yaw command inputs are shown in Figs. 3.15(a) and (b). In order to adjust the  $Y$ -axis wind, yaw command is initially generated to make the vehicle's heading toward wind direction. After that yaw command is changed to turn the vehicle toward the final position. In Fig. 3.15(c), the angle of attack is slightly reduced at 50 to 70 seconds where the maximum dynamic pressure occurs. Since  $Y$ -axis wind is related to the yaw plane, sideslip angle history is significantly different with no wind considering case. In Fig. 3.15(f), the optimized trajectory can reduce aerodynamic load when considering wind, while the aerodynamic load is significantly large when optimization is conducted without wind. The optimized trajectories are shown in Fig. 3.16.

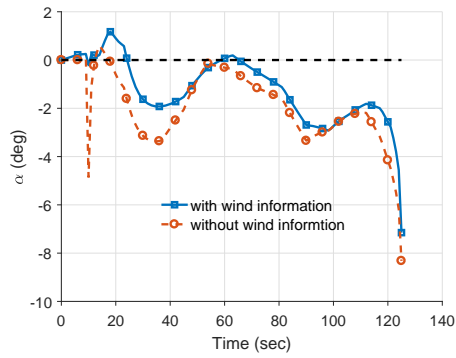
The optimization is conducted with various  $Y$ -axis wind profile in order to find the tendency of the resulting trajectory. The maximum wind velocity is changed as 10,  $-10$ ,  $-30$  and  $-50$  m/s. The results are shown in Figs. 3.17 and 3.18. From the results shown in Figs. 3.17, adjusting  $Y$ -axis wind is more important than  $Z$ -axis wind because  $Y$ -axis velocity of the vehicle is relatively small compared with  $Z$ -axis velocity. Therefore, on the  $Y$ -axis, small wind disturbance can cause a large aerodynamic load to the vehicle.



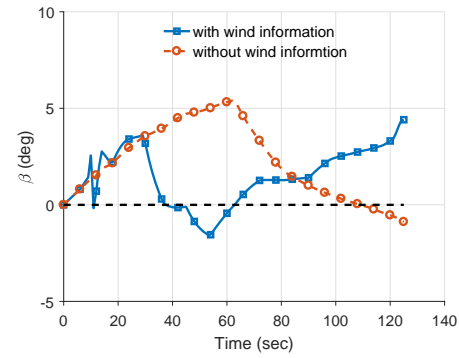
(a) pitch command



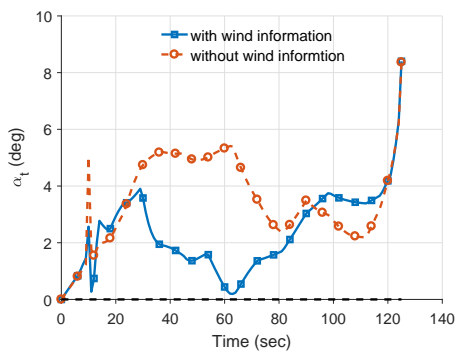
(b) yaw command



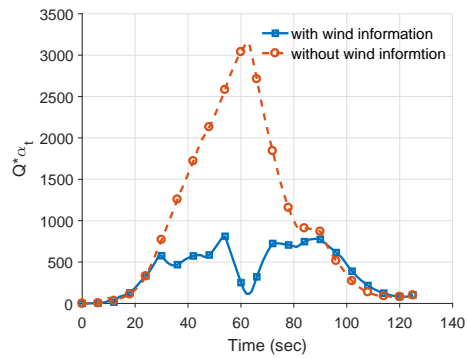
(c) angle of attack



(d) sideslip angle



(e) total angle of attack



(f) aerodynamic load

Figure 3.15: Optimization results of case 3 : Y-axis wind (using 20 nodes)

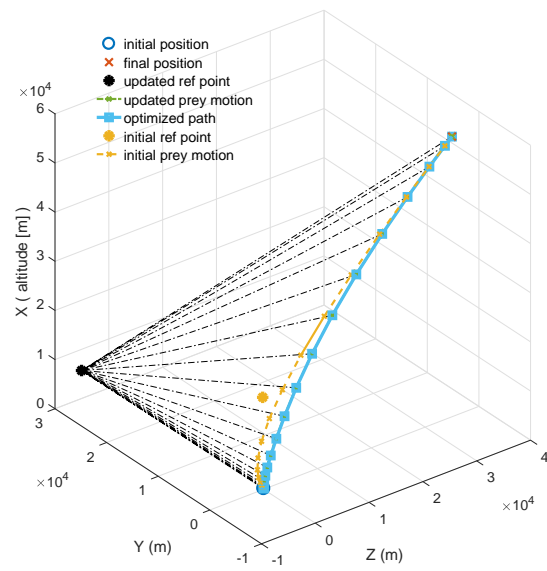
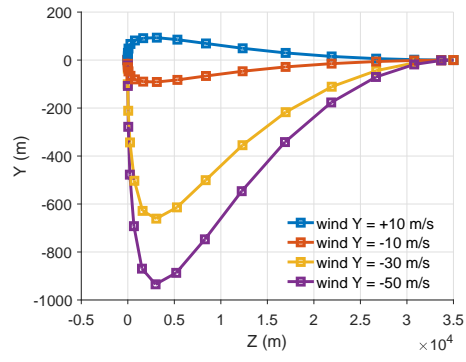
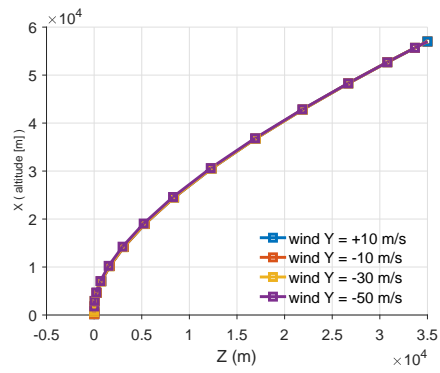


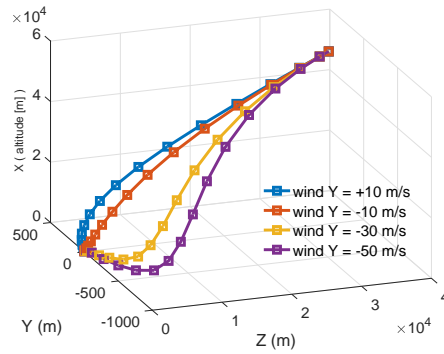
Figure 3.16: Trajectory result of case 3: Y-axis wind (using 20 nodes)



(a) YZ-view

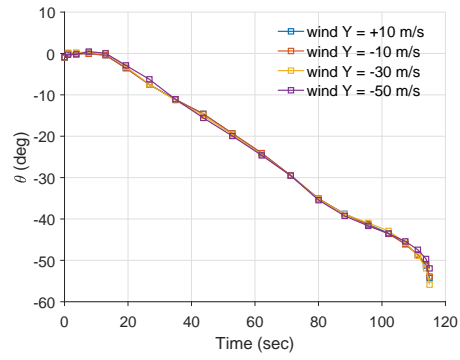


(b) XZ-view

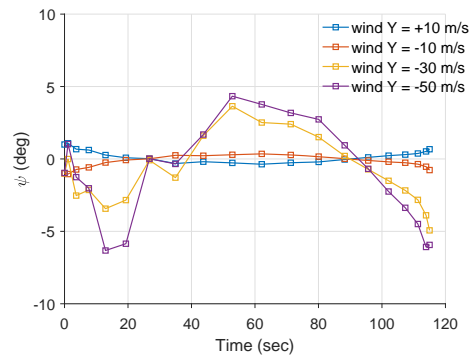


(c) XYZ-view

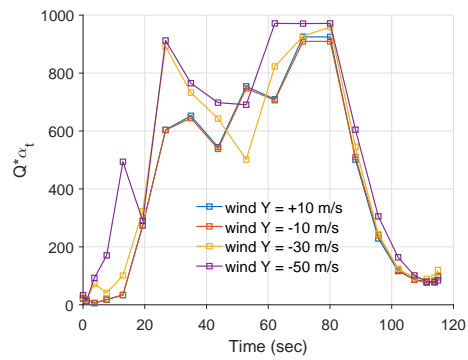
Figure 3.17: Trajectory results of case 3: various Y-axis wind (using 20 nodes)



(a) pitch command



(b) yaw command

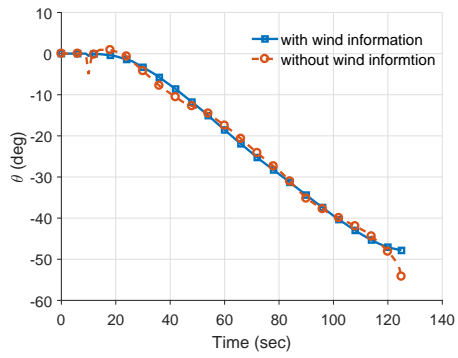


(c) aerodynamic load

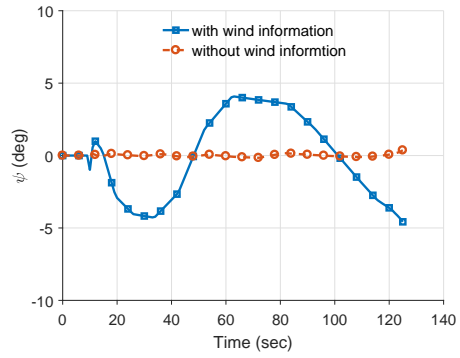
Figure 3.18: Optimization results of case 3: various Y-axis wind (using 20 nodes)

### 3.3.4 Case 4: $Z$ and $Y$ -axes wind disturbance

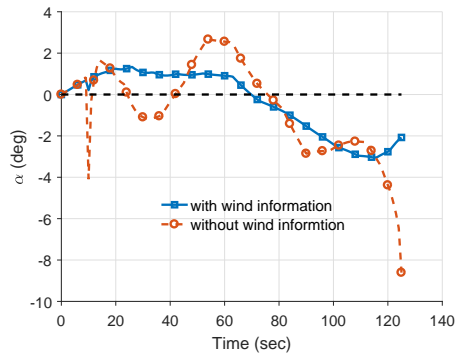
The simulation results with both  $Z$  and  $Y$  axes wind disturbance are examined. The optimization results with 20 nodes are shown in Fig. 3.19 and Fig. 3.20. The results are compared with the result when wind disturbance is not considered. The solid blue lines denote optimization results considering wind disturbance, and the red dashed lines denote results without considering wind disturbance. The simulation results show the composite tendency of previous sections about  $Z$ -axis wind and  $Y$ -axis wind. At this time, both angle of attack and sideslip angles are significantly different with optimization result with no wind considering. The aerodynamic load is significantly large when wind disturbance is not considered.



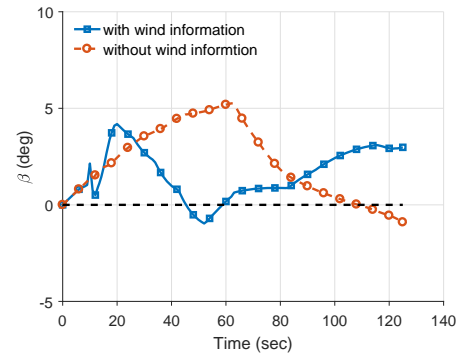
(a) pitch command



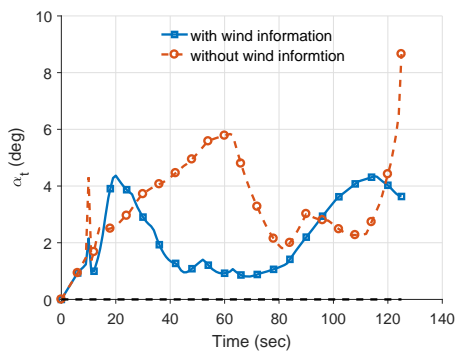
(b) yaw command



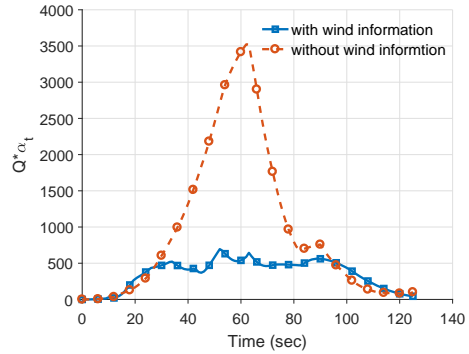
(c) angle of attack



(d) sideslip angle



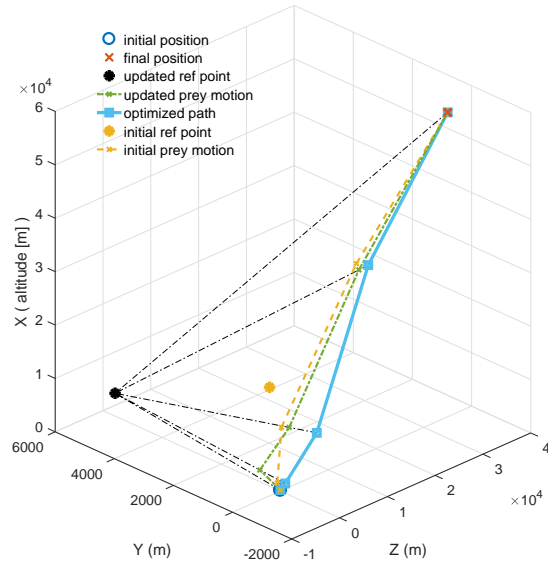
(e) total angle of attack



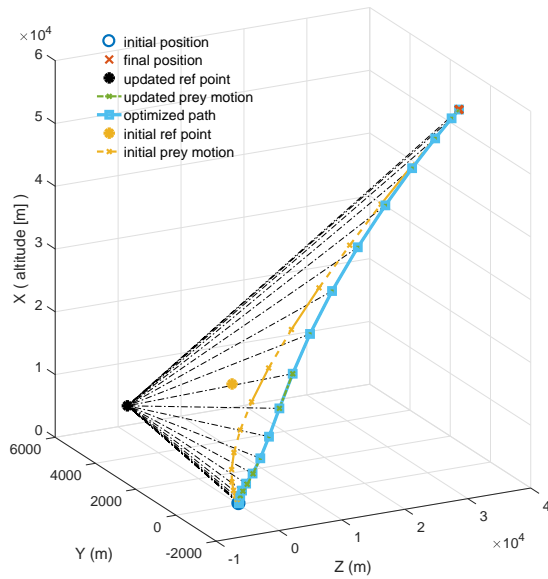
(f) aerodynamic load

Figure 3.19: Optimization results of case 4: Y, Z-axes wind (using 20 nodes)





(a) using 5 nodes



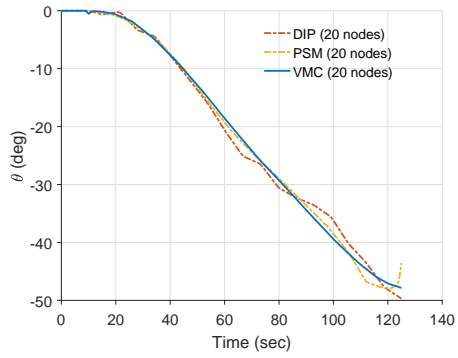
(b) using 20 nodes

Figure 3.20: Trajectory results of case 4: Y, Z-axes wind

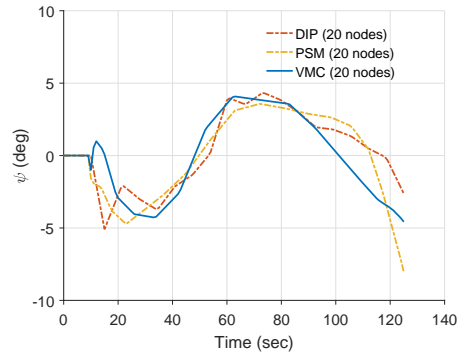
### 3.3.5 Performance comparison

In this subsection, the proposed sequential VMC method is compared with direct input programming (DIP) and pseudospectral method (PSM). The results are analyzed by computational time and cost in Tables. 3.3, 3.4 and 3.5.

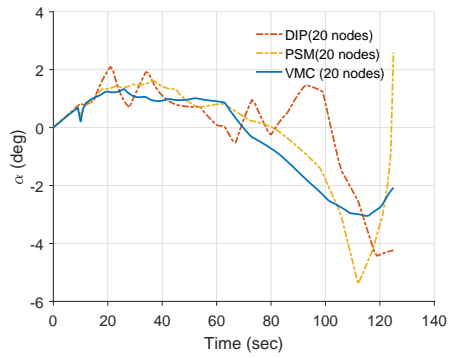
The optimization results using 20 nodes are shown in Figs. 3.21 and 3.22. It is shown that the results from the proposed sequential VMC method are comparable with the two full space methods. The comparison of computational time and cost is summarized in Table. 3.6 and Fig. 3.23. The cost of direct input programming is smaller than VMC, but the tendency of the guidance input and resulting aerodynamic angles are similar. On the other hand, computational time of the VMC is significantly shorter than the other methods.



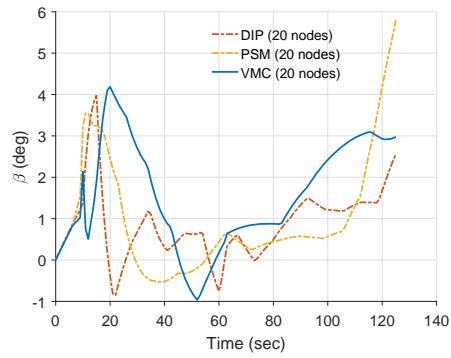
(a) pitch command



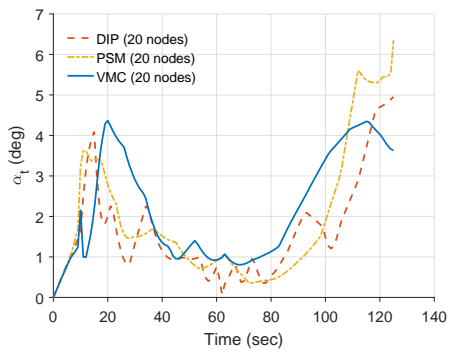
(b) yaw command



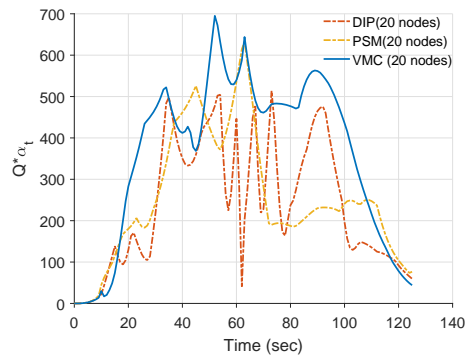
(c) angle of attack



(d) sideslip angle

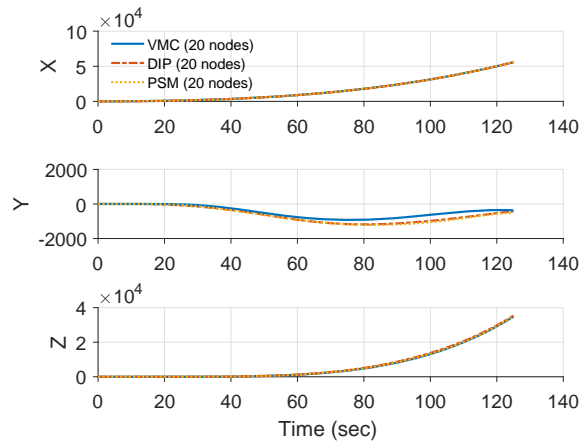


(e) total angle of attack

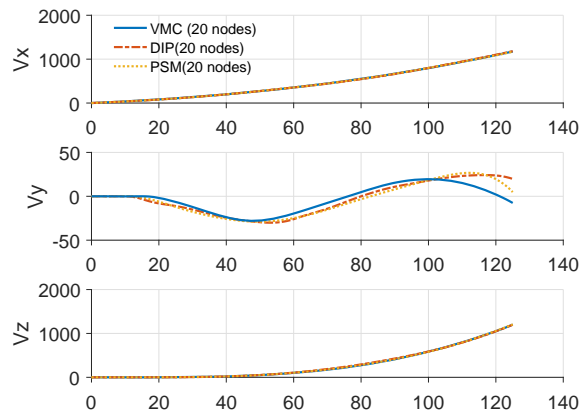


(f) aerodynamic load

Figure 3.21: Optimization result comparison



(a) position



(b) velocity

Figure 3.22: Trajectory comparison

Table 3.3: VMC optimization results

Case 1 : No wind		
Number of nodes	Cost (Pa rad)	Computational time (sec)
5	1000.0	1.14
10	998.3	1.63
15	875.9	2.44
20	852.0	4.80
Case 2 : Z-axis wind		
Number of nodes	Cost (Pa rad)	Computational time (sec)
5	1419.7	0.89
10	990.8	1.46
15	897.0	2.01
20	673.1	4.45
Case 3 : Y-axis wind		
Number of nodes	Cost (Pa rad)	Computational time (sec)
5	1351.7	3.22
10	1218.0	3.64
15	865.8	5.58
20	811.2	6.48
Case 4 : Y,Z-axes wind		
Number of nodes	Cost (Pa rad)	Computational time (sec)
5	1479.6	1.98
10	1191.8	2.62
15	973.2	3.15
20	695.0	6.69

Table 3.4: Direct input programming results

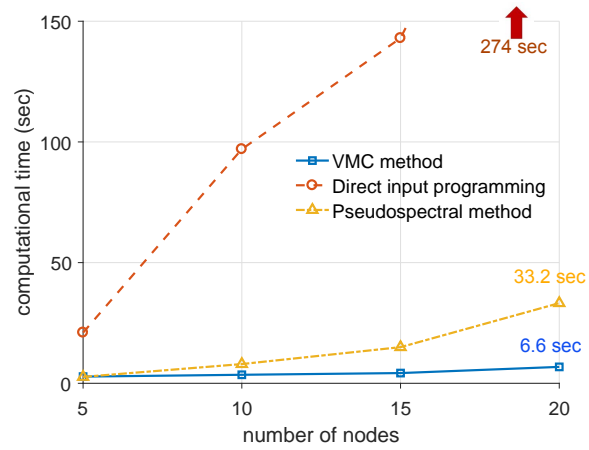
Direct input programming (Case 4 : $Y,Z$ -axes wind)		
Number of nodes	Cost (Pa rad)	Computational time (sec)
5	1981	21
10	1256	97
15	1054	143
20	513	274

Table 3.5: Pseudospectral optimization results

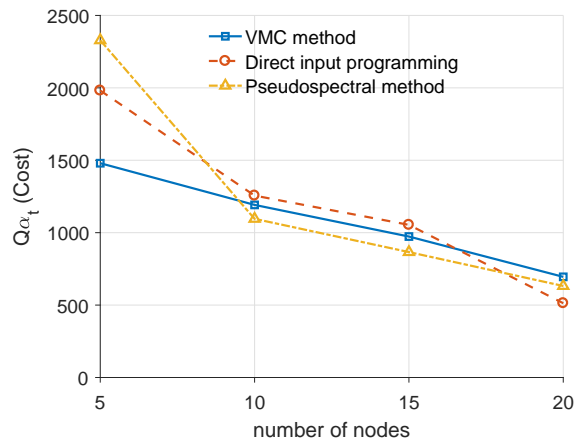
Pseudospectral method (Case 4 : $Y,Z$ -axes wind)		
Number of nodes	Cost (Pa rad)	Computational time (sec)
5	2328.5	2.66
10	1095.6	7.98
15	866.0	14.98
20	635.5	32.22

Table 3.6: Comparison of cost and computational time

	# of nodes	5	10	15	20
Sequential VMC (proposed)	Cost (Pa rad)	1479.6	1191.8	973.2	695.0
	Computational time (sec)	1.98	2.62	3.15	6.69
Pseudospectral method	Cost (Pa rad)	2328.5	1095.6	866.0	635.5
	Computational time (sec)	2.66	7.98	14.98	32.22
Direct input programming	Cost (Pa rad)	1981	1256	1054	513
	Computational time (sec)	21	97	143	274



(a) computational time



(b) cost

Figure 3.23: Comparison of results

# 4

## Robust Control

Modern launch vehicles are becoming long and slender for the reduction in structure mass to increase payload. As a result, they possess highly flexible bending modes in addition to aerodynamically unstable rigid body characteristics. In order to stabilize the unstable rigid system, a feedback controller with a sufficient gain should be designed, but such control system has the potential to excite lightly damped poles of the flexible bending modes [2]. Furthermore, parameters defining the launch vehicle system such as unstable pole and natural frequencies of bending modes are highly uncertain. Therefore, one of the main challenges of a control system for a launch vehicle is to stabilize this unstable interaction in the presence of substantial uncertainty and disturbance. At the same time, sufficient response speed is also demanded. The main part of the study will be conducted for the pitch axis.

### **4.1 Launch vehicle model description**

---

In this section, the dynamic model of the launch vehicle and its properties are described. The launch vehicle system can be divided into the rigid body part and the flexible body



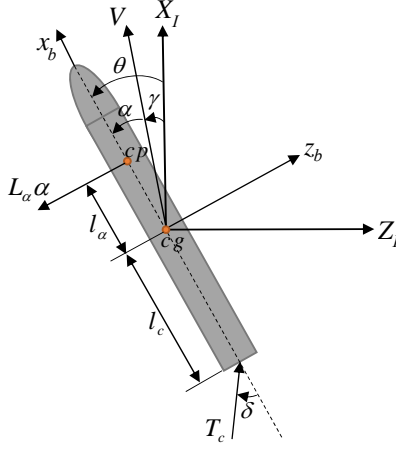


Figure 4.1: Launch vehicle model in the pitch plane

part [41]. After describing each part, the actuator is modeled and its effect to the launch vehicle system including rigid body and bending modes will be explained.

### 4.1.1 Rigid body model

The rigid body model in the pitch plane is shown in Fig. 4.1. The short period dynamics of the rigid body model in the pitch plane can be obtained using the following moment equation:

$$\begin{aligned} \ddot{\theta} &= \left( \sum M_y \right) / I_{yy} \\ &= (L_\alpha l_\alpha \alpha + T_c l_c \delta) / I_{yy} = \mu_\alpha \alpha + \mu_c \delta \end{aligned} \quad (4.1)$$

where  $\alpha = \theta - \gamma$  is the angle of attack,  $\theta$ ,  $\gamma$ ,  $T_c$  and  $\delta$  are the pitch angle, flight path angle, controlled thrust force and thruster angle deflection, respectively. For the purpose of this paper, which is to stabilize an unstable and flexible system with large uncertainties, we consider a simplified rigid body model by assuming that  $\alpha \approx \theta$  and the output of the

sensor is  $\theta$  only [42, 43]:

$$G_r(s) = \frac{\theta}{\delta} = \frac{\mu_c}{s^2 - \mu_\alpha} \quad (4.2)$$

The rigid body part Eq. (4.2) is aerodynamically unstable because the center of mass lies aft of the center of pressure. We consider the rigid body model linearized at the most significant dynamic pressure point which has an unstable pole with the largest modulus [43]. The values linearized at this point are obtained as  $\mu_\alpha = 3.22$  and  $\mu_c = 7.07$ , and both parameters have the uncertainty of  $\pm 10\%$ .

### 4.1.2 Flexible modes and Actuator

In this study, we take into account the first three flexible bending modes due to the roll-off by the actuator bandwidth beyond such frequency. The effect of bending modes can be modeled by adding perturbation angle at the pitch angle  $\theta$  as shown in Fig. 4.2. The flexible body model is obtained by summation of the first three flexible modes:

$$G_f(s) = \frac{\theta_b}{\delta} = \sum_{i=1}^3 G_{f,i} . \quad (4.3)$$

Each flexible bending mode is modeled as a second-order system with natural frequency  $\omega_{n,i}$  and damping  $\zeta_i$ :

$$G_{f,i}(s) = \frac{\theta_{b,i}}{\delta} = \frac{K_i}{s^2 + 2\zeta_i\omega_{n,i}s + \omega_{n,i}^2} \quad (4.4)$$

where  $\theta_{b,i}$  is the perturbation pitch angle due to bending vibration.  $K_i$  is the DC gain of the  $i$ -th bending mode. Typically, the bending modes are lightly damped  $\zeta_i \ll 1$ . As a result, the launch vehicle dynamics including rigid body Eq. (4.2) and flexible modes Eq. (4.3) for

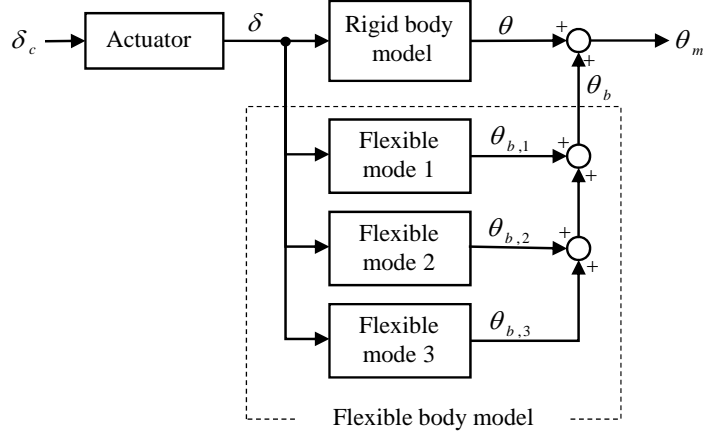


Figure 4.2: Block diagram of the launch vehicle with the rigid body and flexible body parts

Table 4.1: The uncertainty range of the  $i$ -th flexible bending mode

Parameter	Description	Uncertainty range
$K_i$	DC gain	$\pm 40$ %
$\omega_{n,i}$	Natural frequency	$\pm 25$ %
$\zeta_i$	damping	$\pm 30$ %

the pitch axis can be represented as

$$\theta_m = \theta + \theta_b = (G_r(s) + G_f(s)) \delta . \quad (4.5)$$

Since it is very difficult to obtain the parameters of the flexible bending modes such as natural frequency and damping precisely, they have significant uncertainties. The uncertain ranges considered in this paper are listed in table 4.1.

The Bode plot of the launch vehicle model Eq. (4.5) with uncertain parameters is shown in Fig. 4.3 as blue lines. Since the system has one unstable pole from the rigid body model, the phase starts from  $-180$  degree. The flexible bending modes produce phase lag at the natural frequencies of each bending mode, which results in very low phase margins. Therefore, very small delay such as actuator dynamics can cause an unstable interaction with flexible bending modes. For that reason, the actuator dynamics have to be included

in the system model to be controlled. The actuator is modeled as the second-order system :

$$G_{act}(s) = \frac{\delta}{\delta_c} = \frac{\omega_{act}^2}{s^2 + 2\zeta_{act}\omega_{act}s + \omega_{act}^2} \quad (4.6)$$

where  $\omega_{act}$  and  $\zeta_{act}$  are the natural frequency and the damping of the actuator. As a result, the entire system to be controlled is expressed as

$$G_p(s) = \frac{\theta_m}{\delta_c} = (G_r(s) + G_f(s)) G_{act}(s) . \quad (4.7)$$

The Bode plot of the launch vehicle with actuator dynamics Eq. (4.7) is shown in Fig. 4.3 as red lines. Now the first bending mode becomes unstable because its natural frequency is close to the bandwidth of the actuator. The entire system Eq. (4.7) can be represented as the following state-space form:

$$\begin{aligned} \dot{x} &= Ax + B\delta_c \\ \theta_m &= Cx \end{aligned} \quad (4.8)$$

where  $x = [\dot{\theta} \ \theta \ \dot{\theta}_{b,1} \ \theta_{b,1} \ \dot{\theta}_{b,2} \ \theta_{b,2} \ \dot{\theta}_{b,3} \ \theta_{b,3} \ \dot{\delta} \ \delta]^T$ ,  $A \in \mathcal{R}^{10 \times 10}$ ,  $B \in \mathcal{R}^{10 \times 1}$ ,  $C \in \mathcal{R}^{1 \times 10}$ .

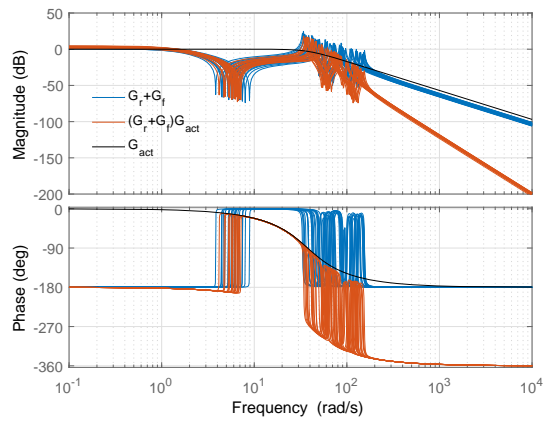


Figure 4.3: Bode plot of the launch vehicle w/ and w/o actuator dynamics

### 4.1.3 System properties and design specifications

The root locus of the launch vehicle with actuator dynamics Eq. (4.7) is shown in Fig. 4.4. As explained in the previous section, when the actuator is considered, an unstable interaction arises between the unstable rigid body and first flexible bending mode. This unstable interaction causes following control problem:

In order to stabilize unstable poles of the rigid body part, a feedback controller with sufficient gain should be designed, but such feedback control system has the potential to excite lightly damped poles of the first bending mode, which destabilizes the system. To make matters worse, the parameters of rigid body model and flexible modes are highly uncertain. Therefore, one of the main challenges is to stabilize the launch vehicle which has unstable interaction with large parameter uncertainties.

The objective of the control system is to provide sufficient margins for the unstable rigid body and improved response speed of the closed-loop. Also, the control system should be robust to the parameter uncertainty and disturbance with small tracking error. All controllers including baseline controllers and robust controller are designed to have at least -6 dB gain reduction margin for unstable rigid body and at least 25 deg phase margin. The robust stability is tested by using mu-analysis [44].

In this study, we design an  $H_\infty$  controller to satisfy the above objectives. Typically, the  $H_\infty$  robust control gives conservative results when large uncertainty is considered due to the small-gain theorem. Therefore, we aim to design  $H_\infty$  controller with sufficient tracking performance while maintaining robust stability in Section 4.3.

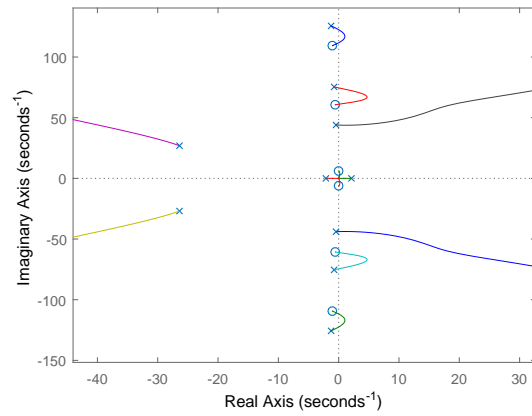


Figure 4.4: Root locus of the launch vehicle with actuator dynamics Eq. (4.7)

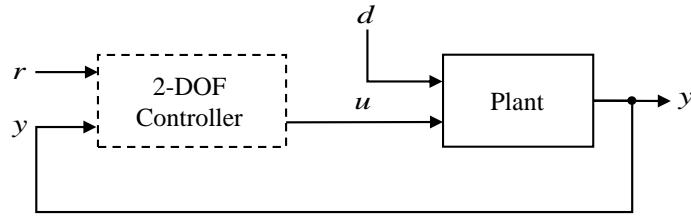


Figure 4.5: General 2-DOF control structure

## 4.2 Baseline controllers design

---

In this section, the baseline controllers are designed by linear optimal control . Usually, the optimal control gives a satisfactory nominal performance such as sufficient steady-state error and response speed. We use the result of the optimal control as a target closed-loop of the robust controller for the enhancement of the nominal performance.

We found that various 1-DOF controllers which use  $e = y - r$  as a feedback signal fail to achieve the satisfactory tracking performance and robustness simultaneously. Thus, all of the baseline controllers and  $H_\infty$  controller are designed with a 2-DOF structure which uses the reference command  $r$  and output feedback signal  $y$  separately. This structure results in feedforward control in addition to feedback control as illustrated in Fig. 4.5. Here a set-point LQG and an integral LQG are designed as a 2-DOF optimal control approach, and their results are examined.

### 4.2.1 Set-point LQG

The set-point LQG control structure is shown in Fig. 4.6. The control input  $u = \delta_c$  consists of feedforward and feedback control inputs as

$$u = Nr - K\hat{x} \tag{4.9}$$



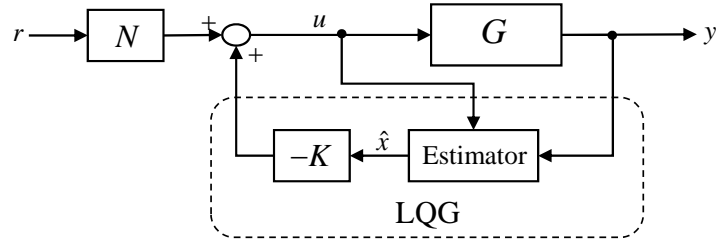


Figure 4.6: Set-point LQG control structure

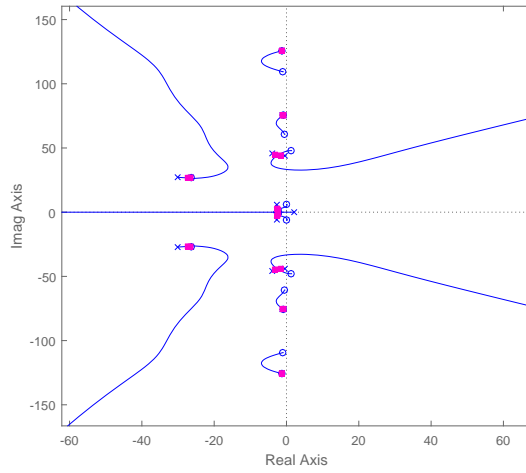


Figure 4.7: Root locus of set-point LQG

where  $K$  and  $N$  are the feedback gain and the feedforward gain, respectively.  $\hat{x}$  is the estimation of the states from output  $y$ . The feedforward control gain  $N$  is derived as follows: By assuming that  $y = r$  at the steady state ( $\dot{x} = 0$ ), the system equation Eq. (4.8) with control input Eq. (4.9) becomes

$$\begin{aligned} 0 &= (A - BK)x_{ss} + BNr \\ y &= Cx_{ss} = r \end{aligned} \quad (4.10)$$

Rearranging the above equations against feedforward control gain  $N$  yields

$$N = -(C(A - BK)^{-1}B)^{-1} \quad (4.11)$$

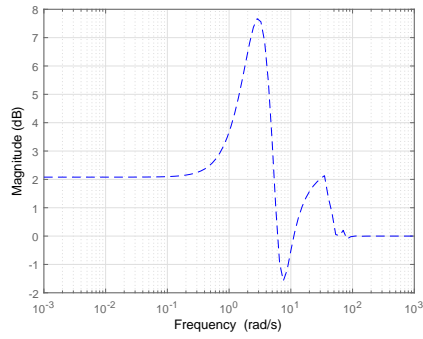
Then designed set-point LQG can be expressed as a general 2-DOF control structure which uses reference  $r$  and output  $y$  separately as shown in Fig. 4.5 by the following state-space form:

$$\dot{\hat{x}} = (A - BK - LC)\hat{x} + \begin{bmatrix} BN & L \end{bmatrix} \begin{bmatrix} r \\ y \end{bmatrix} \quad (4.12)$$

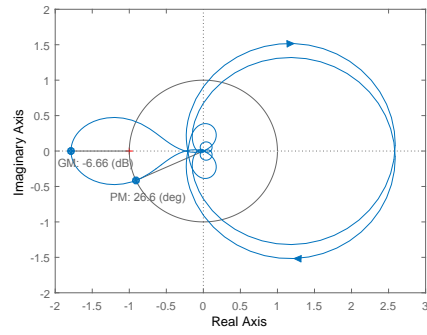
$$u = -K\hat{x} + \begin{bmatrix} N & 0 \end{bmatrix} \begin{bmatrix} r \\ y \end{bmatrix} \quad (4.13)$$

where  $K$  is the optimal control gain of the LQR and  $L$  is the Kalman filter gain.  $N$  is the constant feedforward gain defined in Eq. (4.11).

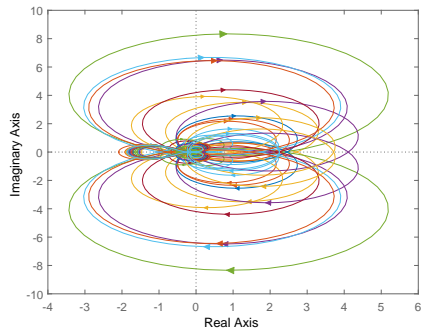
The properties of the designed set-point LQG are examined by root-locus as shown in Fig. 4.7. It can be seen that LQG consists of a lead-compensator to stabilize the unstable pole and a notch-filter for the first bending mode to handle the unstable interaction. The various control synthesis results are illustrated in Fig. 4.8. The sensitivity function is shown in Fig. 4.8(a). Here, we can see that magnitude at the low-frequency is quite large, directly proportional to disturbance attenuation and steady-state error performance. This is because set-point LQG does not possess an integral effect. The Nyquist diagram is illustrated in Fig. 4.8(b). Since we consider the unstable plant, the Nyquist plot of the closed-loop system encircles -1 once. The gain reduction margin for the unstable pole is  $-6.66$  dB, and minimum phase margin is  $26.6$  deg. The large circle at the right side denotes the first bending mode. Although the magnitude of the first bending mode is larger than 1, notch filter turns bending modes away from  $-1$ . Fig. 4.8(c) represents the Nyquist plot of the perturbed plants which sampled within given uncertainty range. Here, we can see that the first bending mode invades the critical point  $-1$ , and destabilizes the closed-loop system. This result can be interpreted as the inappropriateness of a notch filter to handle flexible bending modes when large uncertainty is involved. The step response of the nominal plant is shown in Fig. 4.8(d) and step responses of the uncertain plants are shown in Fig. 4.8(e). The result of the mu-analysis is represented in Fig. 4.8(f). As expected, the closed-loop



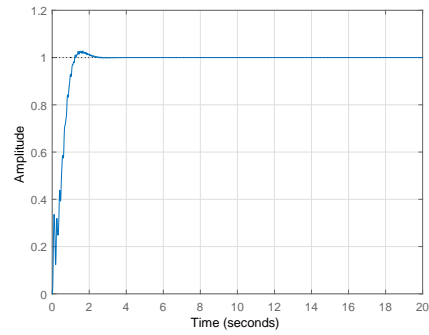
(a) Sensitivity function



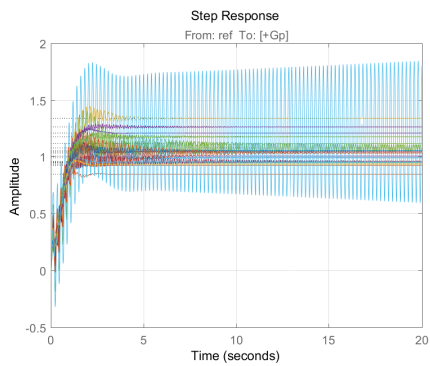
(b) Nyquist plot of nominal plant



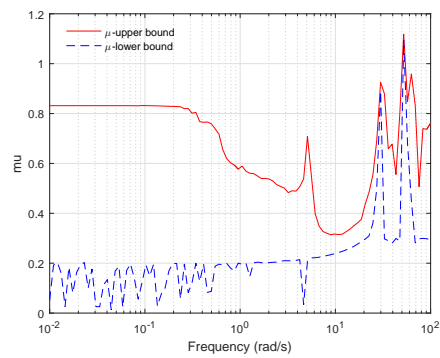
(c) Nyquist plot of uncertain plants



(d) Step response of nominal plant



(e) Step responses of uncertain plants



(f) Robust stability

Figure 4.8: Simulation results of the set-point LQG

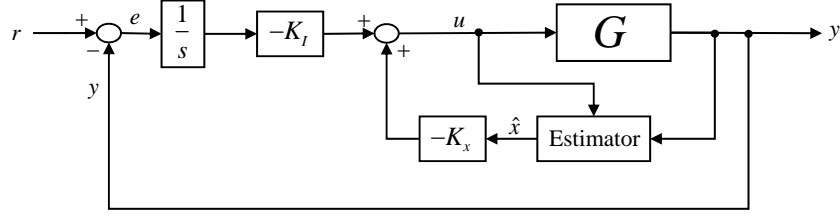


Figure 4.9: LQI control structure

system is not robustly stable. Furthermore, since the set-point LQG does not possess an integral effect, the closed-loop system will be fragile to disturbance such as wind gust and DC gain uncertainty of the system. Therefore, LQG with an integral effect will be designed in the next section.

### 4.2.2 Integral LQG

The structure of the LQG augmented with integral error control is shown in Fig. 4.9. This control structure is referred as LQI in this paper. In order to derive the LQI control input, we define the augmented states  $\tilde{x} = \begin{bmatrix} \dot{x} & e \end{bmatrix}^T$ , where  $e = r - y$ . Then dynamics of the augmented state  $\tilde{x}$  can be derived in the following state space form :

$$\begin{bmatrix} \ddot{x} \\ \dot{e} \end{bmatrix} = \begin{bmatrix} 0 & A \\ 0 & -C \end{bmatrix} \begin{bmatrix} e \\ \dot{x} \end{bmatrix} + \begin{bmatrix} B \\ 0 \end{bmatrix} \dot{u} \quad (4.14)$$

$$\dot{\tilde{x}} = \tilde{A}\tilde{x} + \tilde{B}\nu \quad (4.15)$$

Here,  $\nu = \dot{u}$  is obtained by optimal control theory as

$$\nu = \dot{u} = -\tilde{K}\tilde{x} = - \begin{bmatrix} K_x & K_I \end{bmatrix} \begin{bmatrix} \dot{x} \\ e \end{bmatrix} \quad (4.16)$$

Then the control input  $u$  can be obtained by integrating  $\dot{u}$

$$u = -K_x x - K_I \int_0^t e \, dt \quad (4.17)$$

The designed LQI can be expressed as a general 2-DOF control structure by the following state-space form:

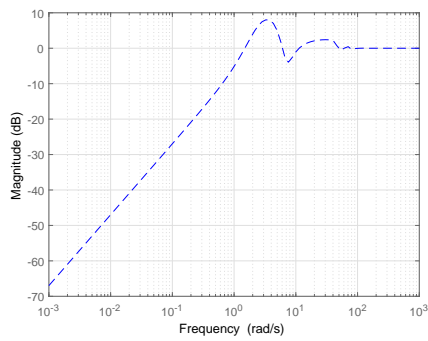
$$\begin{aligned} \begin{bmatrix} \dot{\hat{x}} \\ e \end{bmatrix} &= \begin{bmatrix} A - BK_x - L_I C & -BK_I \\ 0 & 0 \end{bmatrix} \begin{bmatrix} \hat{x} \\ \int_0^t e \, dt \end{bmatrix} \\ &+ \begin{bmatrix} 0 & L_I \\ I & -I \end{bmatrix} \begin{bmatrix} r \\ y \end{bmatrix} \\ u &= - \begin{bmatrix} K_x & K_I \end{bmatrix} \begin{bmatrix} \hat{x} \\ \int_0^t e \, dt \end{bmatrix} + \begin{bmatrix} 0 & 0 \end{bmatrix} \begin{bmatrix} r \\ y \end{bmatrix} \end{aligned} \quad (4.18)$$

where  $L_I$  is the Kalman filter gain.  $K_x$  and  $K_I$  are obtained by minimizing the following cost function for regulating error:

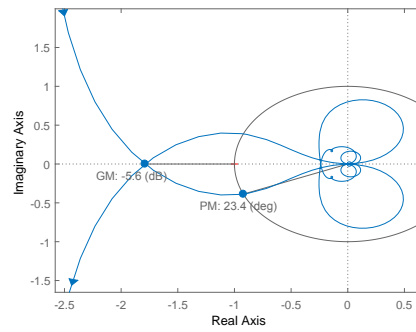
$$PI_1 = \int_0^\infty (e^T P e + \nu^T R \nu) \, dt \quad (4.19)$$

The results of the control synthesis are illustrated in Fig. 4.10. The sensitivity function with integral effect is shown in Fig. 4.10(a). The Nyquist diagram is illustrated in Fig. 4.10(b). The gain reduction margin for the unstable pole is  $-5.6$  dB, and minimum phase margin is  $23.4$  deg. The result of the mu-analysis is represented in Fig. 4.10(c). The designed LQI gives poor robust stability in the low-frequency region as well as the high-frequency region where bending modes are excited. The step responses of the uncertain plants diverge as shown in Fig. 4.10(d).

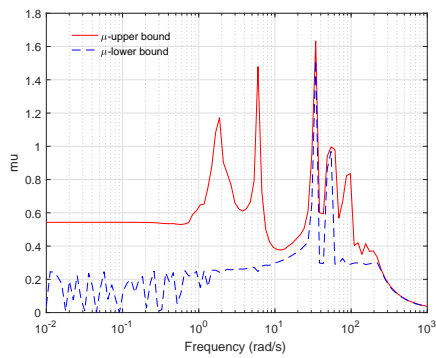
In order to improve the robustness of the LQI, control gains  $K_x$  and  $K_I$  are adjusted



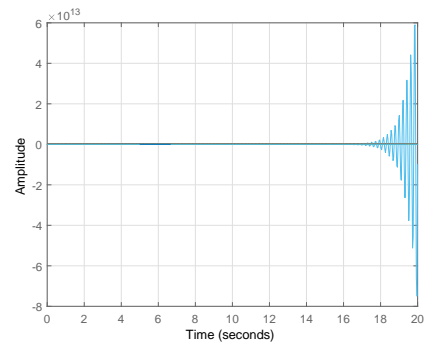
(a) Sensitivity function



(b) Nyquist plot of nominal plant



(c) Robust stability



(d) Step responses of uncertain plants

Figure 4.10: Simulation results of the LQI with  $PI_1$

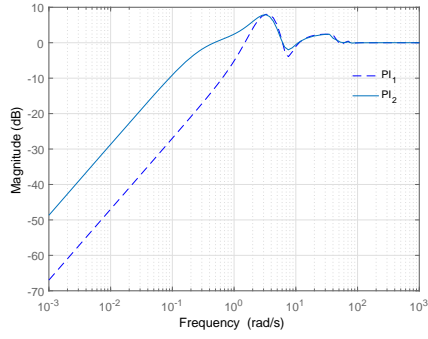
by redefining the performance index as

$$PI_2 = \int_0^{\infty} (e^T P_1 e + \dot{y}^T P_2 \dot{y} + \nu^T R \nu) dt \quad (4.20)$$

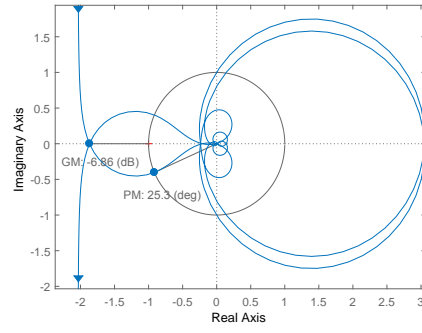
Here, regulation of  $\dot{y}$  is added to improve robustness.  $P_1$ ,  $P_2$  and  $R$  are positive weighting constants.

The synthesis results with redefined performance index Eq. (4.20) are illustrated in Fig. 4.11. The sensitivity function is shown in Fig. 4.11(a). Here we can see that the slope of the gain curve at the crossover frequency (0 dB) is attenuated, which results in enhancement of robustness. The Nyquist diagram is illustrated in Fig. 4.11(b). The gain reduction margin for the unstable pole is  $-6.86$  dB and minimum phase margin is  $25.3$  deg. Fig. 4.11(c) represents the Nyquist plot of the perturbed plants sampled within the given uncertainty range. Here, we can see that the first bending mode invades the critical point  $-1$ , and destabilizes the closed-loop system. The step response of the nominal plant is shown in Fig. 4.11(d). The speed of the response is reduced because the crossover frequency of the sensitivity function has been decreased as shown in Fig. 4.11(a). The step responses of the uncertain plants are shown in Fig. 4.11(e). Some perturbed plants are destabilized by the first bending mode. The result of the mu-analysis is represented in Fig. 4.11(f). By adjusting the performance index, robust stability is improved in the low-frequency region but does not satisfy robust stability in the high-frequency region where the flexible bending modes are excited.

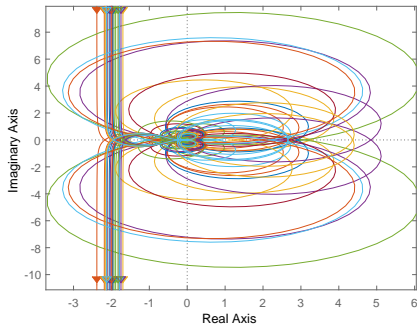
As a summary, the robustness and margins of the closed-loop system are improved by considering  $\dot{y}$  in the cost function of LQI. The main change is the attenuation of the gain slope around the crossover frequency of the sensitivity function. In this respect, the slope of the gain curve around the crossover frequency is essential and milder slope is desirable. Furthermore, since the flexible bending modes have large parametric uncertainty, gain stabilization of the bending modes is desirable rather than phase stabilization. For this, the control system should roll-off below natural frequency of the first bending mode.



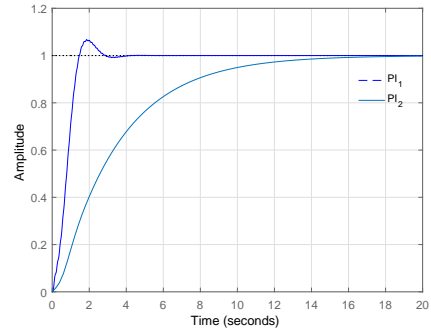
(a) Sensitivity function



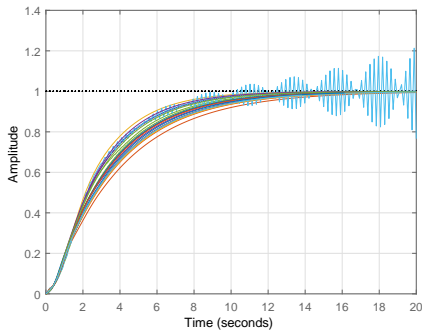
(b) Nyquist plot of nominal plant



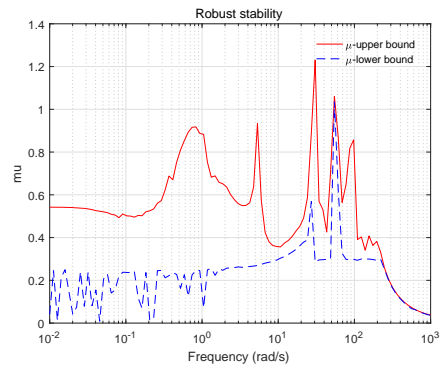
(c) Nyquist plot of uncertain plants



(d) Step response of nominal plant



(e) Step responses of uncertain plants



(f) Robust stability

Figure 4.11: Simulation results of the LQI with  $PI_2$



## 4.3 Robust controller design

---

In this section, a 2-DOF  $H_\infty$  controller is designed. In order to achieve desirable behavior of the closed-loop system, frequency-dependent weights, which are used to shape closed-loop transfer functions, have to be well designed. For this, it is necessary to have an idea of the desired closed-loop shape of the controlled system. First, we try to design a robust controller with conventional weighting functions for shaping the sensitivity function and the control bandwidth. Next, we modify weighting functions, by reflecting the desirable closed-loop shape from the results of LQI, to achieve improved performance without loss of robustness.

### 4.3.1 $H_\infty$ control theory

A control system is robust if it remains stable in the presence of uncertainties. The small-gain theorem plays an important role in the  $H_\infty$  control theory [44].

**Theorem 1** (Small-gain theorem). *Assume that two stable systems  $G_1(s)$  and  $G_2(s)$  are connected in a feedback loop, then the closed-loop system is input-output stable if*

$$\|G_1(s)G_2(s)\|_\infty < 1 \text{ and } \|G_2(s)G_1(s)\|_\infty < 1$$

$H_\infty$  norm is convenient for representing unstructured uncertainty, and also it satisfies the multiplicative property such as

$$\|A(s)B(s)\|_\infty \leq \|A(s)\|_\infty \cdot \|B(s)\|_\infty$$

A linear system with uncertain dynamics can be represented as Fig. 4.12. Here,  $\Delta$  is unstructured uncertainty and assumed stable.  $M$  is the nominal closed-loop system with the feedback controller  $K$ . Then, from the small-gain theorem and multiplicative property of the  $H_\infty$  norm, the closed-loop system is robustly stable if and only if  $K$  stabilize the

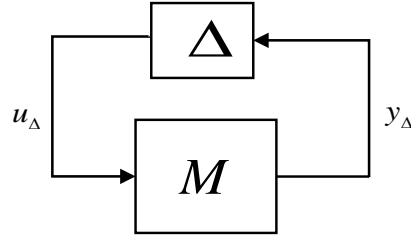


Figure 4.12: Closed-loop system with uncertainty

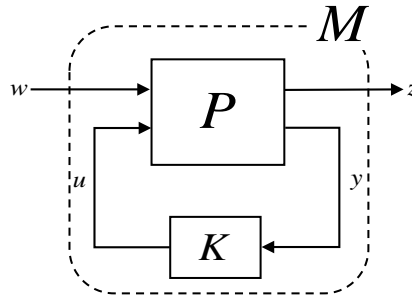


Figure 4.13: Controller synthesis framework

nominal plant and the following holds

$$\|M\Delta\|_\infty \leq \|M\|_\infty \cdot \|\Delta\|_\infty < 1 \quad (4.21)$$

$$\|M\|_\infty < \frac{1}{\|\Delta\|_\infty} \quad (4.22)$$

For a control synthesis, the general framework takes the form of Fig. 4.13. Closing the feedback control loop, let the transfer function of the input  $w$  to the output  $z$  be  $T_{zw}$ . The  $H_\infty$  control problem is then to find a controller  $K$  that makes the closed loop system stable and that minimize  $\|T_{zw}\|_\infty$ .

$$\min_K \|T_{zw}\|_\infty \quad (4.23)$$

For analysis purpose, closed-loop  $M$  can be connected with given uncertainty as Fig. 4.14.

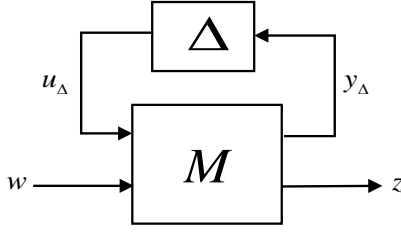


Figure 4.14: Analysis framework

The structured singular value  $\mu$  is defined with structured uncertainty by

$$\mu(M) \triangleq \frac{1}{\min_{\Delta \in \mathbf{\Delta}} \{\bar{\sigma}(\Delta) : \det(I - M\Delta) = 0\}} \quad (4.24)$$

$\mu$  value can be interpreted as the inverse of the smallest magnitude of a destabilizing perturbation of  $M$  [44]. Thus the structured singular value provides an indicator of how much uncertainty can be tolerated before the system become unstable.

### 4.3.2 Two-degree-of freedom $H_\infty$ controller

The 2-DOF structure for the synthesis of the  $H_\infty$  controller is shown in Fig. 4.15. The controller  $K = \begin{bmatrix} K_r & K_y \end{bmatrix}^T$  consists of a feedforward controller  $K_r$  for shaping the command to improve tracking performance and a feedback controller  $K_y$  for stabilizing the uncertain plant and disturbance rejection. The important transfer functions can be derived from Fig. 4.15 as follows:

$$y = \left( \frac{G(s)K_r(s)}{1 - G(s)K_y(s)} \right) r + \left( \frac{1}{1 - G(s)K_y(s)} \right) d \quad (4.25)$$

$$u = \left( \frac{K_r(s)}{1 - G(s)K_y(s)} \right) r + \left( \frac{K_y(s)}{1 - G(s)K_y(s)} \right) d \quad (4.26)$$

where  $G(s)$  is the nominal plant of  $G_p$  (Eq. (4.7)).

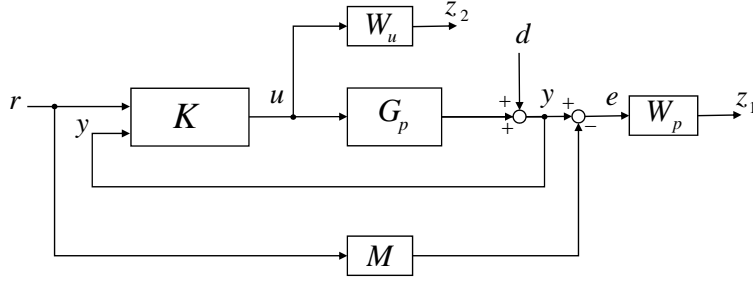


Figure 4.15: 2-DOF  $H_\infty$  control structure with model reference

The control error  $e = y - M(s)r$  can be rewritten as

$$e = \left( \frac{G(s)K_r(s)}{1 - G(s)K_y(s)} - M(s) \right) r + \left( \frac{1}{1 - G(s)K_y(s)} \right) d \quad (4.27)$$

From Eq. (4.27),  $K_y$  is designed for adjusting the system poles and disturbance, and  $K_r$  is for improving tracking performance from  $r$  to  $e$ . As a result, the closed-loop transfer function matrix from external input  $w = \begin{bmatrix} r & d \end{bmatrix}^T$  to  $z = \begin{bmatrix} z_1 & z_2 \end{bmatrix}^T$  can be derived as

$$T_{zw} = \begin{bmatrix} z_1 \\ z_2 \end{bmatrix} = \begin{bmatrix} W_p(SGK_r - M) & W_pS \\ W_uSK_r & W_uK_yS \end{bmatrix} \begin{bmatrix} r \\ d \end{bmatrix} \quad (4.28)$$

where  $S$  is the sensitivity function defined as  $S = 1/(1 - G(s)K_y(s))$ .  $W_p$  and  $W_u$  are the frequency-dependent weighting functions to shape the closed-loop transfer functions of  $T_{zw}$  to satisfy complex objectives such as robust stability and tracking performance. After weights are selected, the controller  $K$  is obtained such that  $\|T_{zw}\|_\infty$  is minimized.

### 4.3.3 Selection of weighting functions: $W_p$ and $W_u$

The selection of weighting functions is the most important step in the robust controller design process because the weighting functions define the desirable closed-loop behavior in the robust control synthesis. Since performance objectives are mainly related to the sensitivity function, the performance weight  $W_p$  has to be designed to reflect performance

requirements. For good tracking performance, the magnitude of the sensitivity transfer function  $S$  has to be minimized. Since tracking performance and disturbance rejection are important at low frequencies, the sensitivity function  $S$  is minimized in this range. To this end,  $W_p$  is usually defined as [45, 36]

$$W_{p1} = \frac{s/M_S + \omega_b}{s + \omega_b \epsilon_S} \quad (4.29)$$

where  $M_S$ ,  $\omega_S$  and  $\epsilon_S$  are the lower bound of the maximum singular value, bandwidth and steady-state error of  $S$ , respectively.  $M_S$  is related to classical margins by [44]

$$GM \geq \frac{M_S}{M_S - 1}, \quad PM \geq \frac{1}{M_S}.$$

After fine tuning to satisfy the robust stability, we selected  $M_S = 3$ ,  $\omega_S = 0.8$  rad/s and  $\epsilon_S = 0.5$ . The resulting  $W_{p1}$  acts as a low-pass filter.

In order to attenuate the flexible bending modes in the high-frequency region, the control sensitivity function  $K(s)S(s)$  is limited by using a high-pass filter defined as

$$W_{u1} = \left( \frac{s/\sqrt[k]{M_u} + \omega_u}{s + \omega_u \sqrt[k]{\epsilon_u}} \right)^k \quad (4.30)$$

Here,  $M_u$ ,  $\omega_u$ ,  $\epsilon_u$  and  $k$  are lower bounds of the maximum singular value, bandwidth, roll-off magnitude and roll-off rate of  $K(s)S(s)$ , respectively. We chose  $M_u = 10$  to limit low-frequency control gain, and  $\omega_u = 25$  to limit control bandwidth in the high-frequency region where bending modes may be excited. The roll-off magnitude is defined as  $\epsilon_u = 0.01$ . In order to roll-off as fast as possible beyond the control bandwidth, we selected  $k = 3$  for  $W_{u1}$ .

As mentioned before, the robustness and margins of the closed-loop system can be improved by considering  $\dot{y}$  in the cost function of LQI. Such result can be reflected in the robust control design by augmenting additional performance output  $z_3 = \dot{y}$  as shown in

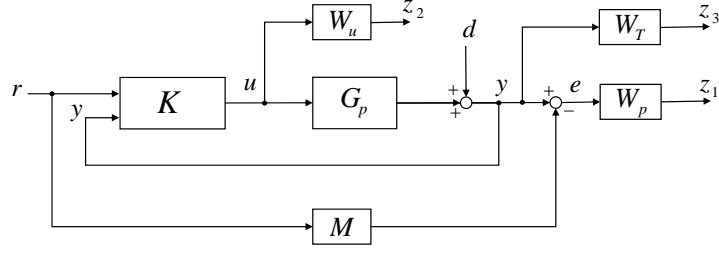


Figure 4.16: 2-DOF  $H_\infty$  control structure augmented by  $z_3$

Fig. 4.16. Then the closed-loop transfer function matrix under consideration is changed to

$$T_{\bar{z}w} = \begin{bmatrix} z_1 \\ z_2 \\ z_3 \end{bmatrix} = \begin{bmatrix} W_p(SGK_r - M) & W_pS \\ W_uSK_r & W_uK_yS \\ W_TSGK_r & W_TS \end{bmatrix} \begin{bmatrix} r \\ d \end{bmatrix} \quad (4.31)$$

where  $W_T$  is the weighting function for  $z_3$ . The augmentation of  $y$  results in the increased dimension of the transfer function and may lead to a more conservative controller due to the definition of the  $H_\infty$ -norm.

Instead, we can reflect the effect of regulating  $\dot{y}$  by defining the sensitivity weighting function obtained from the analysis of the LQI, i.e., adding  $\dot{y}$  in the cost function results in attenuation of the slope around the crossover frequency of the sensitivity function. Therefore, we designed another performance weighting function which has different slopes in the low frequency region and around the crossover frequency as

$$W_{p2} = \frac{s^2 + 3.511s + 0.5178}{2.884s^2 + 2.027s + 0.01546} \quad (4.32)$$

To limit control bandwidth,  $W_{u2}$  is designed as

$$W_{u2} = \left( \frac{s / \sqrt[k_2]{M_{u2}} + \omega_{u2}}{s + \omega_{u2} \sqrt[k_2]{\epsilon_{u2}}} \right)^{k_2} \quad (4.33)$$

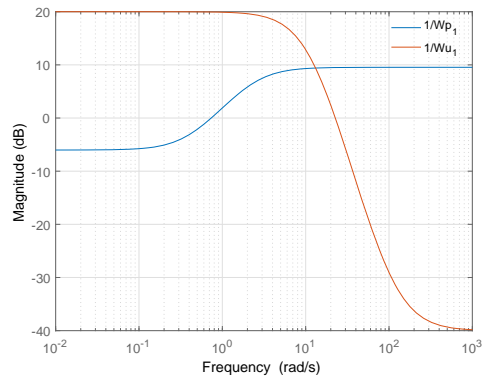
with the parameters  $M_{u2} = 10$ ,  $\omega_{u2} = 20$ ,  $\epsilon_{u2} = 0.01$  and  $k_2 = 3$ . The designed weighting

functions are represented in Fig. 4.17.

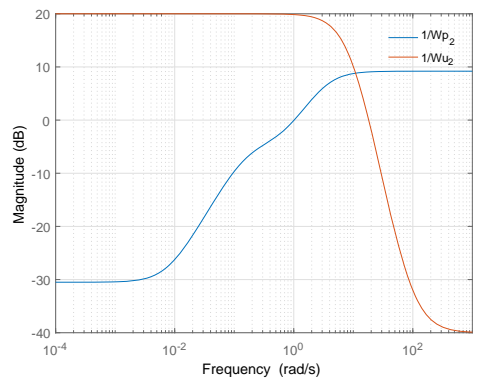
The model reference is chosen as a second-order system:

$$M(s) = \frac{\omega_n^2}{s^2 + 2\zeta\omega_n s + \omega_n^2}.$$

We choose the damping of the model reference as  $\zeta = 0.9$  and the natural frequency as  $\omega_n = 2$  rad/s.



(a)  $W_{p1}$  and  $W_{u1}$



(b)  $W_{p2}$  and  $W_{u2}$

Figure 4.17: Bode plot of the weighting functions

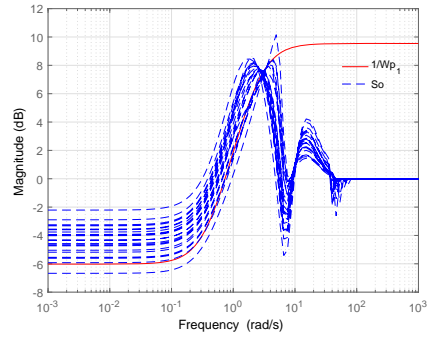


### 4.3.4 Synthesis results

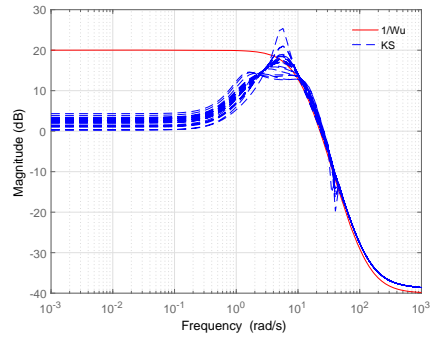
The results of the designed robust controller with conventional weighting function set 1 (i.e.  $W_{p1}$  and  $W_{u1}$ ) are shown in Figs. 4.18 and 4.19. The sensitivity function is shown in Fig. 4.19(a). We can see that magnitude at the low-frequency is quite large, proportional to the disturbance attenuation and the steady-state error performance. The Nyquist diagram is illustrated in Fig. 4.19(b). The gain reduction margin for the unstable pole is  $-6.40$  dB, and minimum phase margin is  $27$  deg. The circle left to the gain reduction margin point is very small, which means the relatively poor performance of steady-state error and disturbance rejection because the magnitude of the sensitivity function in the low frequency is not small enough. The large circle in the right side denotes the first bending mode. Since the robust control tries to roll-off beyond the control bandwidth, the Nyquist plot shows that magnitudes of the bending modes from various perturbed closed-loop systems are contained in the right side as shown in Fig. 4.19(c). The step response of the nominal plant is shown in Fig. 4.19(d) and step responses of the uncertain plants are in Fig. 4.19(e). Although all the sampled closed-loop systems are stable, there exists steady-state error as explained before. The designed controller satisfies robust stability within given uncertainty as shown in Fig. 4.19(f).

The synthesis results of the robust controller with improved weighting function set 2 (i.e.  $W_{p2}$  and  $W_{u2}$ ) are illustrated in Figs. 4.20 and 4.21. The sensitivity function is shown in Fig. 4.21(a). We can see that magnitude at the low-frequency is improved. The Nyquist diagram is illustrated in Fig. 4.21(b). The gain reduction margin for the unstable pole is  $-6.02$  dB, and minimum phase margin is  $25.7$  deg. The circle left to the gain reduction margin point is now large enough for the desired performance of steady-state error and disturbance rejection. Also, the circles are on the right side, which says that the bending modes also become smaller than before. This means that gain stabilization of the bending modes is conducted as well as phase stabilization. In Fig. 4.21(c), the Nyquist plot shows that the magnitudes of the bending modes from various perturbed closed-loop systems are

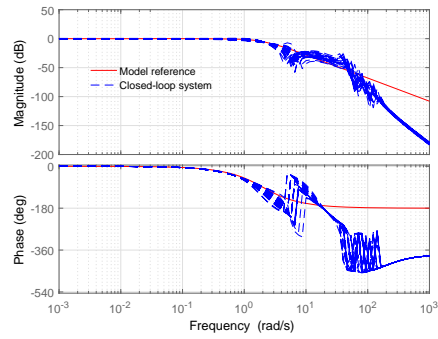
contained in the small region away from the critical point. The step response of the nominal plant is shown in Fig. 4.21(d). The step responses of the uncertain plants are improved as shown in Fig. 4.21(e) while maintaining robust stability as shown in Fig. 4.21(f).



(a) Sensitivity

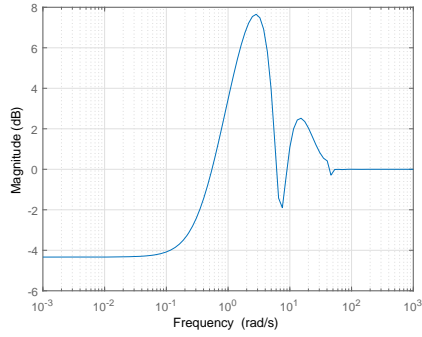


(b) Input sensitivity

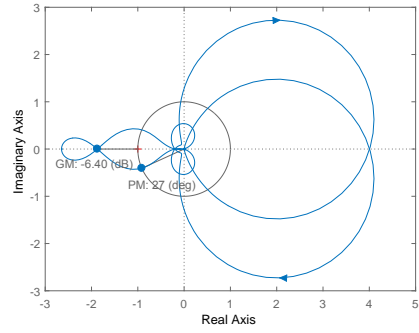


(c) Closed-loop

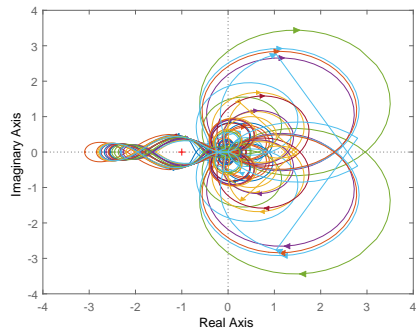
Figure 4.18: Synthesis results of the 2-DOF  $H_\infty$  with  $W_{p1}$  and  $W_{u1}$



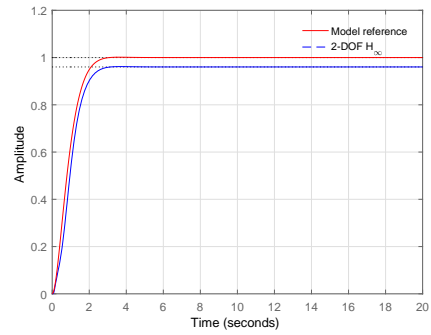
(a) Sensitivity function



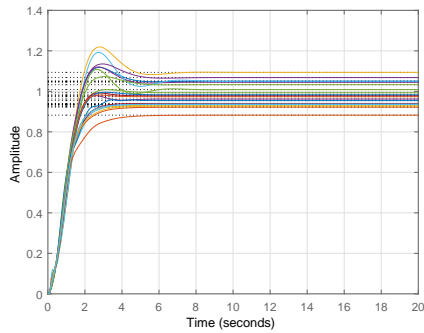
(b) Nyquist plot of nominal plant



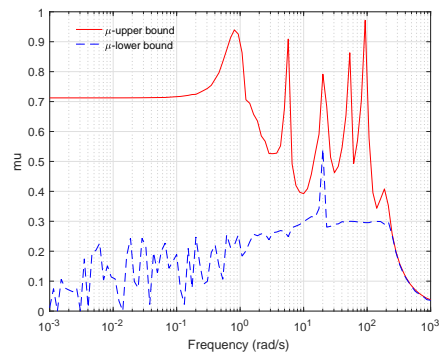
(c) Nyquist plot of uncertain plants



(d) Step response of nominal plant

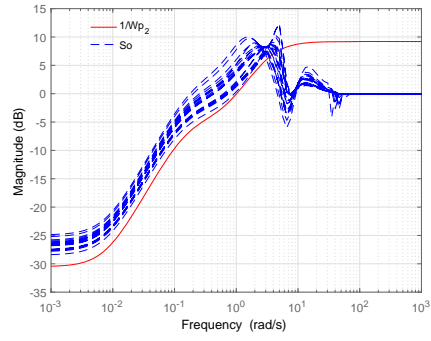


(e) Step responses of uncertain plants

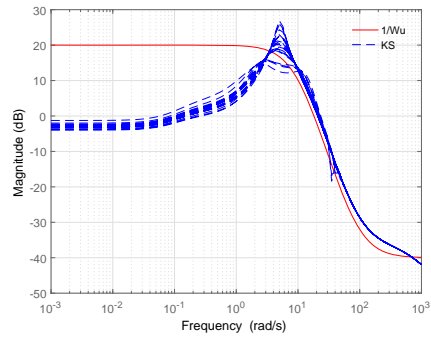


(f) Robust stability

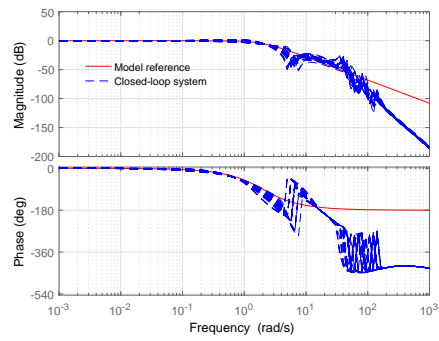
Figure 4.19: Simulation results of the 2-DOF  $H_\infty$  with  $W_{p1}$  and  $W_{u1}$



(a) Sensitivity

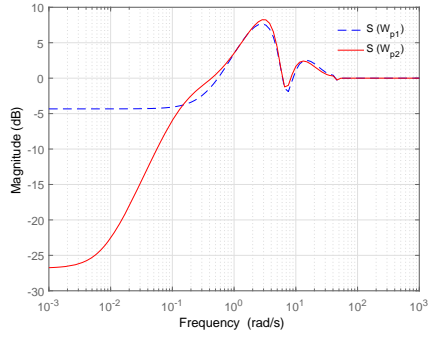


(b) Input sensitivity

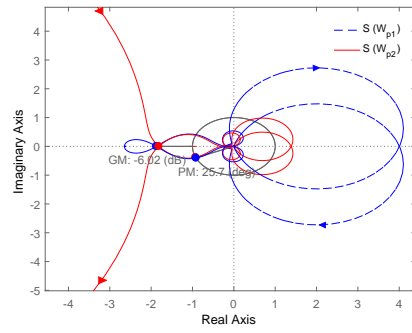


(c) Closed-loop

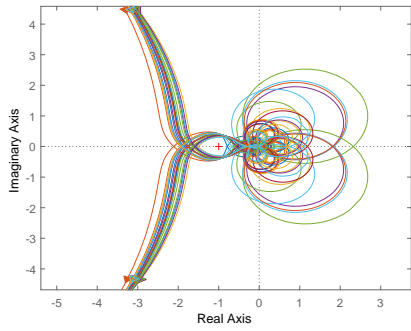
Figure 4.20: Synthesis results of the 2-DOF  $H_\infty$  with  $W_{p2}$  and  $W_{u2}$



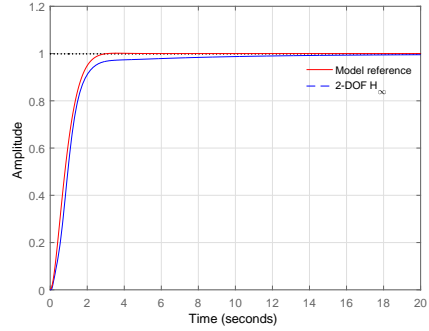
(a) Sensitivity function



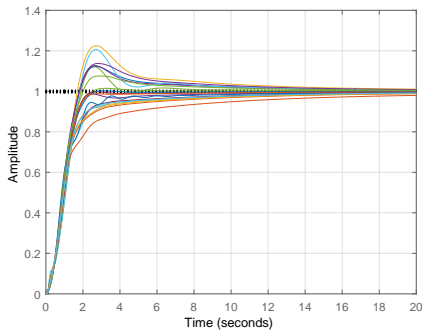
(b) Nyquist plot of nominal plant



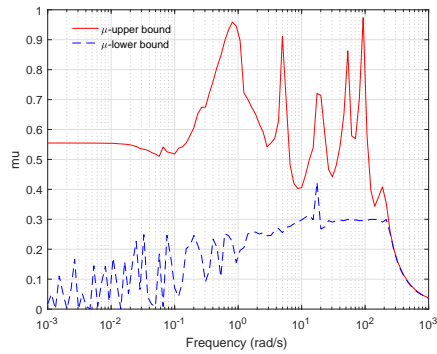
(c) Nyquist plot of uncertain plants



(d) Step response of nominal plant



(e) Step responses of uncertain plants



(f) Robust stability

Figure 4.21: Simulation results of the 2-DOF  $H_\infty$  with  $W_{p2}$  and  $W_{u2}$

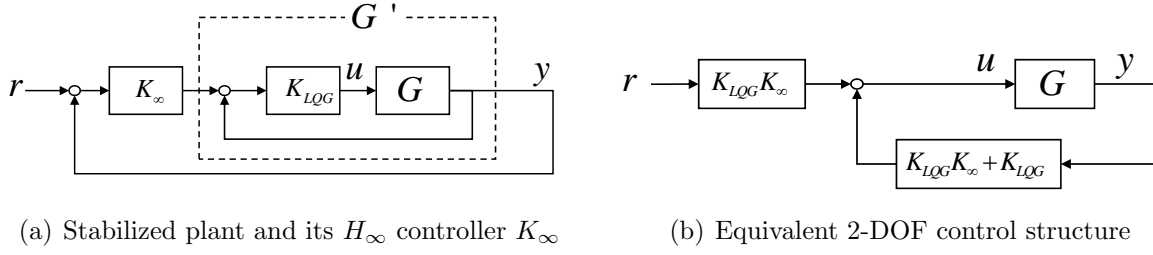


Figure 4.22: Two-loop control structure

### 4.3.5 Comparison study

In this section, a controller used in [36] is examined for comparison study. In [36], to achieve sufficiently robust characteristic, a two-loop control structure is adopted as shown in Fig. 4.22. The original, uncertain plant  $G$  is preliminarily stabilized by using a direct output feedback controller  $K_{LQG}$ . Then the standard  $H_\infty$  controller denoted as  $K_\infty$  is applied to these pre-stabilized plant ( $G'$ ) to improve robustness. This two-loop structure is adopted by the fact that robust control is not always effective in unstable systems.

The above two-loop structure can be rearranged as 2-DOF control structure used in this study by following process:

$$\begin{aligned}
 u &= K_{LQG} [K_\infty (r - y) - y] \\
 &= K_{LQG} K_\infty (r - y) - K_{LQG} y \\
 &= (K_{LQG} K_\infty) r - (K_{LQG} K_\infty + K_{LQG}) y
 \end{aligned} \tag{4.34}$$

The two-loop controller consists of the feedforward controller  $K_{LQG}K_\infty$  and the feedback controller  $K_{LQG}(K_\infty + 1)$  as shown in Eq. (4.34). Therefore, it can be said that this two-loop structure controller is a special case of 2-DOF structure controller.

There, the feedback controller can be divided into  $K_{LQG}$  and  $(K_\infty + 1)$ . At first, the robust controller  $K_\infty$  is designed to stabilize uncertain flexible modes in the high-frequency region. However  $K_\infty$  effect is changed to the combination of  $K_{LQG}$  and  $(K_\infty + 1)$ . As a

result, characteristic of  $K_\infty$  in the high-frequency region such as roll-off effect vanished as shown in Fig. 4.23. This makes the closed-loop system unstable when large uncertainty is incorporated in the high-frequency region.

The result of the two-loop controller is shown in Fig. 4.24. Since the roll-off effect of  $K_\infty$  vanished, the Nyquist plot of the uncertain plant is similar to LQG controller case. As a result, The step response of the uncertain plant diverge, which does not satisfy robust stability. The comparison result of step response is shown in Fig. 4.25. The response of LQI is sluggish compared with 2-DOF  $H_\infty$  and two-loop controller. The two-loop controller response is similar to 2-DOF  $H_\infty$  controller but oscillation occurs. This oscillation is caused by the low gain margin and phase margin. The comparison of the gain margin and phase margin are summarized in table 4.2.



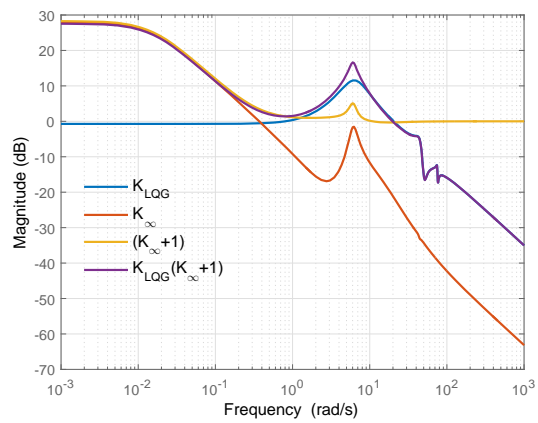
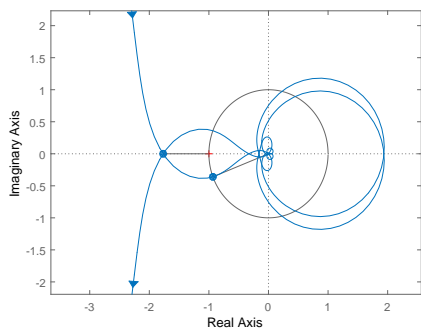
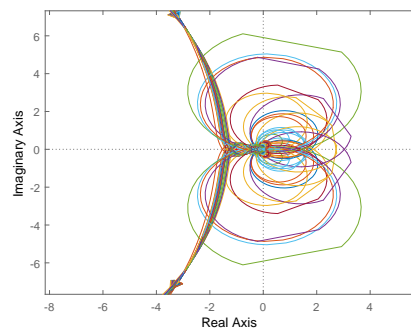


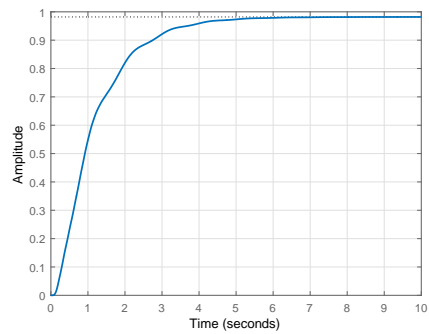
Figure 4.23: Bode plot of two-loop controller



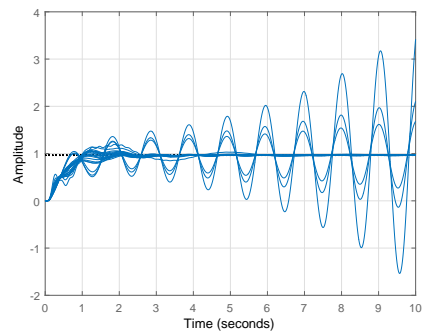
(a) Nyquist plot of nominal plant



(b) Nyquist plot of uncertain plant



(c) Step response of nominal plant



(d) Step response of uncertain plant

Figure 4.24: Synthesis result of two-loop controller

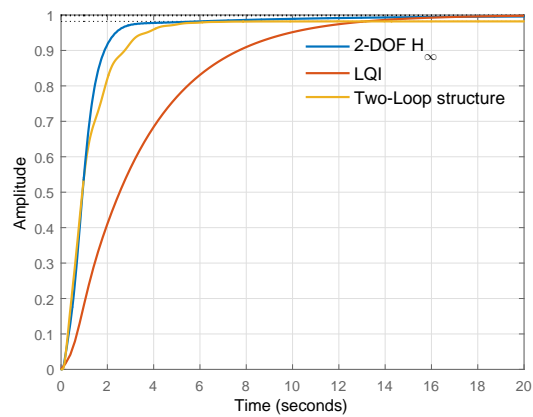


Figure 4.25: Comparison of step response

Table 4.2: Comparison of GM and PM

Nominal case			
Method	Gain reduction margin (dB)	Gain margin (dB)	Phase margin (Deg)
2-DOF $H_\infty$	-6.02	10.14	25.68
LQI	-6.85	12.87	25.3
Two-loop	-4.94	9.66	21.2
Worst case from 50 samples			
Method	Gain reduction margin (dB)	Gain margin (dB)	Phase margin (Deg)
2-DOF $H_\infty$	-4.90	<b>3.21</b>	22.13
LQI	-5.14	<b>-1.54</b>	21.45
Two-loop	-3.24	<b>-0.97</b>	15.27

## 4.4 Numerical simulation

---

Since the system parameters such as mass, thrust and aerodynamic properties vary depending on the time, gain scheduling is necessary to obtain satisfactory closed-loop performance.

A linear time varying system can be represented as parameter dependent system:

$$\begin{aligned}\dot{x} &= A(p)x + B(p)u \\ y &= C(p)x + D(p)u\end{aligned}\tag{4.35}$$

where  $p = (p_1(t), p_2(t), \dots, p_s(t))$  is the scheduling parameter vector. By assuming that the system matrices of Eq. (4.35) are affine in  $p$ , the matrices of the state-space can be represented by affine functions of the parameters as

$$\begin{aligned}A(p) &= A_0 + p_1A_1 + \dots + p_sA_s \\ B(p) &= B_0 + p_1B_1 + \dots + p_sB_s \\ C(p) &= C_0 + p_1C_1 + \dots + p_sC_s \\ D(p) &= D_0 + p_1D_1 + \dots + p_sD_s\end{aligned}$$

where  $A_i, B_i, C_i, D_i$  are constant matrices that do not depend on the parameters.

An affine parameter-dependent system can be converted to an equivalent polytopic system as

$$S(p) = \alpha_1S_1 + \alpha_2S_2 + \dots + \alpha_qS_q, \quad \sum_{i=1}^q \alpha_i = 1, \quad \alpha_i \geq 0$$

In the above expression  $S_1, S_2, \dots, S_q$  are the vertex systems

$$S_i = \begin{bmatrix} A_i & B_i \\ C_i & D_i \end{bmatrix}, \quad i = 1, \dots, q\tag{4.36}$$

and  $\alpha_1, \dots, \alpha_q$  are called the polytopic coordinates of  $S(p)$ . In this way, the polytopic system  $S(p)$  is a convex combination of the system matrices  $S_1, S_2, \dots, S_q$ .

Following above assumptions, the robust controllers are designed at each linearized design point in the corresponding moment of time. The parameter-dependent controller can be represented as

$$K(p) = \begin{cases} \dot{x}_k = A_k(p)x_k + B_k(p)y \\ u = C_k(p)x_k + D_k(p)u \end{cases} \quad (4.37)$$

whose system matrix has the polytopic representation

$$\begin{bmatrix} A_k(p) & B_k(p) \\ C_k(p) & D_k(p) \end{bmatrix} = \sum_{i=1}^q \alpha_i \begin{bmatrix} A_{k,i} & B_{k,i} \\ C_{k,i} & D_{k,i} \end{bmatrix}, \quad \sum_{i=1}^q \alpha_i = 1. \quad (4.38)$$

where  $A_{k,i}, B_{k,i}, C_{k,i}, D_{k,i}$  are the controller system matrices designed at each linearization point  $i$ .

To implement the proposed controller to the launch vehicle dynamics, nine controllers are designed at every fifteen seconds (from 0 to 125 sec). The state-space matrices of the controller at the corresponding flight time are obtained by convex interpolation of the controller set. The singular value plot of the gain-scheduled controller is shown in Fig. 4.26. The result shows that gain-scheduled controller with the vertex representation has smooth singular value through entire operation time. The 6-DOF simulation is conducted to demonstrate gain-scheduled robust controller. The guidance commands are generated before the flight by using sequential VMC. The closed-loop system with the designed robust controller follows the reference input satisfactorily as shown in Fig. 4.27.

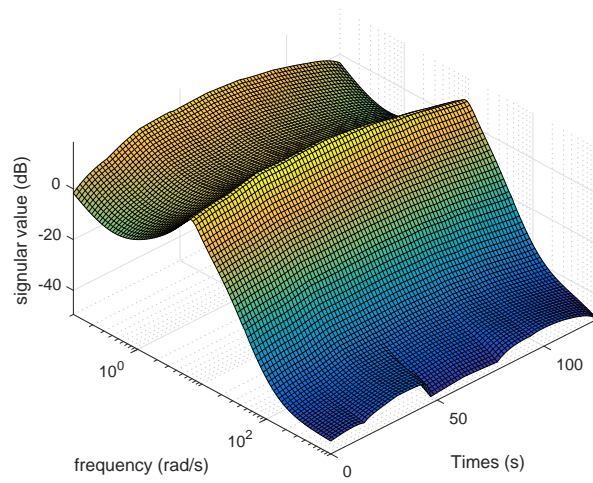
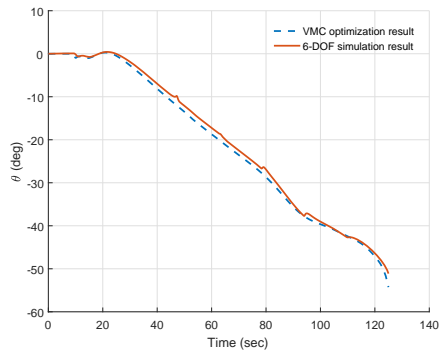
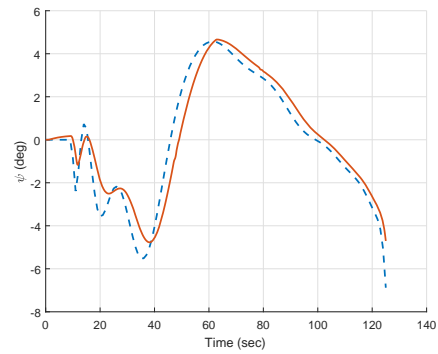


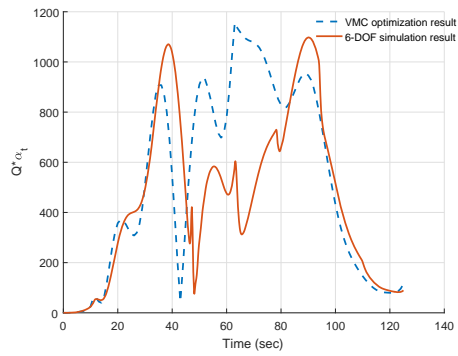
Figure 4.26: Singular value plot of the gain-scheduled controller



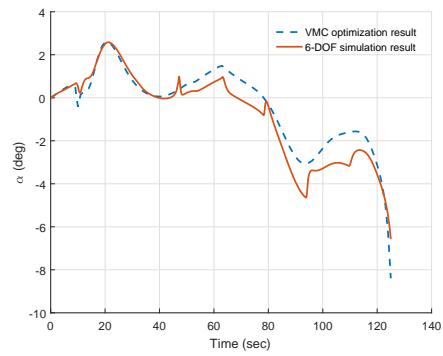
(a) pitch command



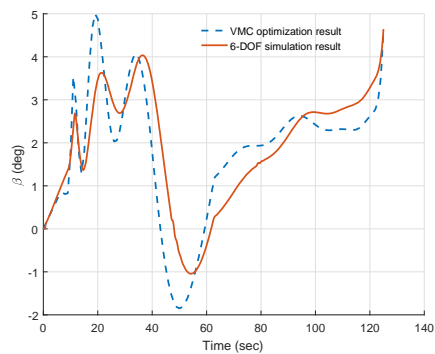
(b) yaw command



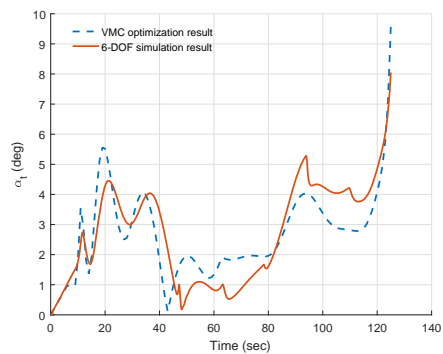
(c) aero load



(d) angle of attack



(e) sideslip angle



(f) total angle of attack

Figure 4.27: 6-DOF simulation results



# 5

## Conclusions

This dissertation proposes a rapid and reliable optimal trajectory generation method and a non-conservative robust controller for the unstable and flexible launch vehicle. The main results of this study are summarized as follows:

- A rapid and reliable optimal trajectory generation method for a launch vehicle is proposed through the utilization of the virtual motion camouflage (VMC). VMC uses a so-called prey motion and reference point to construct a subspace in which the solution trajectory is generated. By the virtue of this subspace search, the overall dimension of the optimization problem is reduced. In practice, this reduction in dimension decreases the computational time significantly compared to traditional direct input programming. Also, in the VMC approach, specific optimal parameters are calculated rather than optimized to satisfy the equality boundary conditions. The fact that no equality constraints are involved in the optimization also makes the convergence easier. In contrast with the indirect method, the parameters to be optimized in the VMC approaches are physically meaningful and defining a reasonable initial guess is not difficult.

- An interactive optimization algorithm is proposed to find a feasible solution easier by adding the constraint correction step. Since the VMC is a subspace problem, the feasible solution may not exist when subspace is not properly constructed. To address this problem, the quadratic programming is formulated to find a direction along which the parameters defining the subspace can be improved. Via a computationally fast quadratic programming, specific parameters (prey and reference point) can be refined quickly and sequentially. As a result, the proposed interactive optimization is insensitive to initial guess of the optimization parameters.
- A non-conservative 2-DOF  $H_\infty$  controller for the unstable and flexible launch vehicle is designed. The objective of the robust control is to provide sufficient margins for the launch vehicle dynamics and to enhance the speed of the closed-loop response. The key of the control design is to overcome conservativeness of the robust control. It is found that 2-DOF control structure which uses feedforward and feedback control together is suitable and adequate for this kind of system. The baseline controllers are designed using the optimal control such as set-point LQG and LQI prior to robust control. In order to see which shape of the sensitivity function is desirable, the different performance indices are defined when designing baseline controllers. After implementation and analysis of the baseline controllers, a non-conventional sensitivity weighting function is devised that has different slopes in the low frequency and around crossover frequency, which results in improvement of the performance without loss of robustness. This result cannot be accomplished using typical weighting functions such as low-pass filter types, as shown in the simulation.

Overall, the integration of the proposed trajectory generation algorithm and the robust controller provides complete guidance and control for a flexible launch vehicle during ascent phase flight.

# References

- [1] W. Du, “Dynamic modeling and ascent flight control of Ares-I crew launch vehicle,” Ph.D. dissertation, Iowa State University, 2010.
- [2] M. Whorton, C. Hall, and S. Cook, “Ascent flight control and structural interaction for the Ares I crew launch vehicle,” *48th AIAA/ASME/ASCE/AHS/ASC Structures, Structural Dynamics, and Materials Conference*, pp. 23–26.
- [3] G. Dukeman, “Atmospheric ascent guidance for rocket-powered launch vehicles,” *AIAA Guidance, Navigation, and Control Conference and Exhibit*, pp. 4559–4556, 2002.
- [4] G. Dukeman and A. Hill, “Rapid trajectory optimization for the Ares I launch vehicle,” *AIAA Guidance, Navigation and Control Conference and Exhibit*, 2008.
- [5] P. Lu, B. J. Griffin, G. A. Dukeman, and F. R. Chavez, “Rapid optimal multiburn ascent planning and guidance,” *Journal of Guidance, Control, and Dynamics*, vol. 31, no. 6, pp. 1656–1664, 2008.
- [6] P. Lu and B. Pan, “Highly constrained optimal launch ascent guidance,” *Journal of Guidance, Control, and Dynamics*, vol. 33, no. 2, pp. 404–414, 2010.
- [7] J. T. Betts, “Survey of numerical methods for trajectory optimization,” *Journal of Guidance, Control, and Dynamics*, vol. 21, no. 2, pp. 193–207, 1998.
- [8] D. H. Hodges, R. R. Bless, A. J. Calise, and M. Leung, “Finite element method for optimal guidance of an advanced launch vehicle,” *Journal of Guidance, Control, and Dynamics*, vol. 15, no. 3, pp. 664–671, 1992.

- [9] R. G. Bruschi, "Trajectory optimization for the Atlas/Centaur launch vehicle," *Decision and Control including the 15th Symposium on Adaptive Processes*, vol. 15, pp. 492–500, 1976.
- [10] J. Speyer, H. Kelley, N. Levine, and W. Denham, "Accelerated gradient projection technique with application to rocket trajectory optimization," *Automatica*, vol. 7, no. 1, pp. 37–43, 1971.
- [11] J. Rea, "Launch vehicle trajectory optimization using a Legendre pseudospectral method," *AIAA Guidance, Navigation, and Control Conference and Exhibit*, 2003.
- [12] B. Yang and S. Sun, "Reentry trajectory optimization of airbreathing hypersonic vehicles based on Gauss pseudospectral method," *Advanced Materials Research*, vol. 383, pp. 7375–7380, 2012.
- [13] A. M. Mahmoud, C. Wanchun, Z. Hao, and L. Yang, "Trajectory optimization for ascent and glide phases using Gauss pseudospectral method," *International Journal of Modeling and Optimization*, vol. 6, no. 5, p. 289, 2016.
- [14] M. V. Srinivasan and M. Davey, "Strategies for active camouflage of motion," *Proceedings of the Royal Society of London. Series B: Biological Sciences*, vol. 259, no. 1354, pp. 19–25, 1995.
- [15] Y. Xu, "Virtual motion camouflage and suboptimal trajectory design," *AIAA Guidance, Navigation and Control Conference and Exhibit*, 2007.
- [16] Y. Xu and G. Basset, "Sequential virtual motion camouflage method for nonlinear constrained optimal trajectory control," *Automatica*, vol. 48, no. 7, pp. 1273–1285, 2012.
- [17] D. J. Kwak, B. Choi, D. Cho, H. J. Kim, and C. W. Lee, "Decentralized trajectory optimization using virtual motion camouflage and particle swarm optimization," *Autonomous Robots*, vol. 38, no. 2, pp. 161–177, 2014.

- [18] N. Imbert and B. Clement, “Launcher attitude control: some answers to the robustness issue,” *16th IFAC Symposium on Automatic Control in Aerospace*, 2004.
- [19] B. Clement, G. Duc, and S. Mauffrey, “Aerospace launch vehicle control: a gain scheduling approach,” *Control Engineering Practice*, vol. 13, no. 3, pp. 333–347, 2005.
- [20] M. Ganet and M. Ducamp, “LPV control for flexible launcher,” *AIAA Guidance, Navigation, and Control Conference*, p. 8193, 2010.
- [21] X. Yang, J. Li, and Y. Dong, “Flexible air-breathing hypersonic vehicle control based on a novel non-singular fast terminal sliding mode control and nonlinear disturbance observer,” *Proceedings of the Institution of Mechanical Engineers, Part G: Journal of Aerospace Engineering*, 2016.
- [22] L. Fiorentini, A. Serrani, M. A. Bolender, and D. B. Doman, “Nonlinear robust adaptive control of flexible air-breathing hypersonic vehicles,” *Journal of Guidance, Control, and Dynamics*, vol. 32, no. 2, pp. 402–417, 2009.
- [23] E. Kharisov, I. Gregory, C. Cao, and N. Hovakimyan, “L1 adaptive control for flexible space launch vehicle and proposed plan for flight validation,” *AIAA Guidance, Navigation and Control Conference and Exhibit*, p. 7128, 2008.
- [24] Y. Lei, C. Cao, E. Cliff, N. Hovakimyan, A. Kurdila, and K. Wise, “L1 adaptive controller for air-breathing hypersonic vehicle with flexible body dynamics,” *American Control Conference*, pp. 3166–3171, 2009.
- [25] C. S. Oh and H. Bang, “Attitude control of flexible launch vehicle using adaptive notch filter,” *IFAC Proceedings Volumes*, vol. 38, no. 1, pp. 187–192, 2005.
- [26] A. Khoshnood, J. Roshanian, and A. Khaki Sedig, “Model reference adaptive control for a flexible launch vehicle,” *Proceedings of the Institution of Mechanical Engineers, Part I: Journal of Systems and Control Engineering*, vol. 222, no. 1, pp. 49–55, 2008.

- [27] D. Alazard, “Robust  $H_\infty$  design for lateral flight control of highly flexible aircraft,” *Journal of Guidance, Control, and Dynamics*, vol. 25, no. 3, pp. 502–509, 2002.
- [28] L. Ou, L. Liu, Y. Wang, and J. Huang, “Observer-based robust control for a flexible launch vehicle,” *Proceedings of the Institution of Mechanical Engineers, Part I: Journal of Systems and Control Engineering*, vol. 229, no. 6, pp. 506–516, 2015.
- [29] J. Bibel and H. Stalford, “ $\mu$ -synthesis autopilot design for a flexible missile,” *29th Aerospace Sciences Meeting*, p. 586, 1991.
- [30] G. J. Balas and J. C. Doyle, “Control of lightly damped, flexible modes in the controller crossover region,” *Journal of Guidance, Control, and Dynamics*, vol. 17, no. 2, pp. 370–377, 1994.
- [31] H. Li, L. Wu, Y. Si, H. Gao, and X. Hu, “Multi-objective fault-tolerant output tracking control of a flexible air-breathing hypersonic vehicle,” *Proceedings of the Institution of Mechanical Engineers, Part I: Journal of Systems and Control Engineering*, vol. 224, no. 6, pp. 647–667, 2010.
- [32] M. Abbas Turki, G. Duc, and B. Clement, “Multi-objective controller design for a space launcher,” *Control Conference*, pp. 4016–4022, 2007.
- [33] B. Clement and G. Duc, “A multi-objective control algorithm: Application to a launcher with bending modes,” *Proceedings of the 8th IEEE Mediterranean Conference on Control and Automation*, 2000.
- [34] A. A. Khalate, A. Naseer, S. Jose, and M. Dhekane, “Multi-objective control of aerodynamically unstable launcher,” *Control & Automation*, pp. 1–6, 2007.
- [35] R. A. Wright and C. Kravaris, “Two-degree-of-freedom output feedback controllers for nonlinear processes,” *Chemical Engineering Science*, vol. 60, no. 15, pp. 4323–4336, 2005.

- [36] Y. Morita and J. Kawaguchi, “Attitude control design of the M-V rocket,” *Philosophical Transactions of the Royal Society of London A: Mathematical, Physical and Engineering Sciences*, vol. 359, no. 1788, pp. 2287–2303, 2001.
- [37] Y. Morita, “An idea of applying  $\mu$ -synthesis to launcher attitude and vibration control design,” *Modal Analysis*, vol. 10, no. 9, pp. 1243–1254, 2004.
- [38] F. Fahroo and I. M. Ross, “Costate estimation by a Legendre pseudospectral method,” *Journal of Guidance, Control, and Dynamics*, vol. 24, no. 2, pp. 270–277, 2001.
- [39] G. Oh, J. Park, J. Park, H. Lee, Y. Kim, S.-J. Shin, J. Ahn, and S. Cho, “Load relief control of launch vehicle using aerodynamic angle estimation,” *Proceedings of the Institution of Mechanical Engineers, Part G: Journal of Aerospace Engineering*, 2017.
- [40] N. Ishii and H. Yamakawa, “Pitch angle program modification due to wind shear in MV rocket first stage ascent trajectory,” *Proceedings of the 8th Workshop on Astrodynamics and Flight Mechanics*, pp. 183–188, 1997.
- [41] W. Du, B. Wie, and M. Whorton, “Dynamic modeling and flight control simulation of a large flexible launch vehicle,” *AIAA Guidance, Navigation and Control Conference and Exhibit*, p. 6620, 2008.
- [42] D. Navarro Tapia, A. Marcos, S. Bennani, and C. Roux, “Structured  $H_\infty$  control based on classical control parameters for the VEGA launch vehicle,” *IEEE Conference on Control Applications*, pp. 33–38, 2016.
- [43] E. Gadea Díaz, *Design of a robust controller for the VEGA TVC using the  $\mu$ -synthesis technique*. Universitat Politècnica de Catalunya, 2010.
- [44] S. Skogestad and I. Postlethwaite, *Multivariable feedback control: analysis and design*. Wiley, 2007, vol. 2.

[45] K. Zhou and J. C. Doyle, *Essentials of robust control*. Prentice Hall, 1998.



# 국 문 초 록

본 논문에서는 발사체의 상승구간 동안의 구조하중 최소화를 위한 궤적 최적화와 유연한 효과를 고려한 강건 제어기 설계에 관한 연구를 수행하였다. 상승구간 동안에 발사체는 큰 공력 하중에 노출되므로 이를 고려한 최적 궤적 생성이 중요하다. 특히 동압이 매우 큰 영역에서는 바람과 같은 외란이 심각한 요인으로 작용한다. 뿐만 아니라 최근의 발사체는 구조하중을 줄이고 유효하중을 높이기 위해서 길고 가느다란 형상을 가진다. 그로인해 발사체는 공력학적으로 불안정한 강체모델과 벤딩모드를 포함하게 되므로 이를 고려할 수 있는 제어기가 필요하다.

본 논문에서는 virtual motion camouflage (VMC) 기법을 적용한 최적 궤적 생성기법과 불안정하고 유연한 발사체를 제어하기 위한 강건 제어기법을 제안하였다.

첫 번째로, VMC 기법을 이용하여 계산시간이 적게 걸리면서도 신뢰할 수 있는 최적 궤적을 생성하였다. VMC 기법은 자연계에서 포식자가 자신이 들키지 않는 상태로 먹잇감을 쫓아가는 모습에서 영감을 얻어 고안된 방법이다. 먹잇감과 기준점 개념을 도입하여 부분 공간을 구성하게 되고, 이 부분 공간 위에서 최적 해를 찾게 된다. VMC에서 포식자의 궤적은 path control parameter (PCP) 라는 스칼라 값으로 표현할 수 있게 된다. 이러한 개념의 도입으로 3차원 궤적 생성문제가 1차원 스칼라 최적화 문제로 바뀌게 된다. 결과적으로 이러한 차원의 감소를 통해 전통적인 경로 최적화 방법들 보다 매우 빠르게 경로를 생성 할 수 있게 하였다.

두 번째로 순차적으로 최적화를 수행하는 기법을 제안하여 feasible한 해를 항상 찾을 수 있게 하였다. Constraint correction (CC) 단계를 VMC 최적화 다음에 수행하여 먹잇감과 기준점으로 표현되는 부분공간을 개선하게 하였다. 이는 부분공간에서 해를 찾는 VMC기법을 보완하기 위해 수행된 것으로, 부분공간이 제약조건을 만족하는 해를 포함하고 있지 않을 경우 부분공간을 업데이트 하는 방법이다. 제약조건을 만족하는 해를 포함하는 방향으로 부분공간을 업데이트 하였고, 업데이트 방향은 quadratic programming (QP) 문제를 풀어 구할 수 있게 하였다. 제안된 방법은 QP의 빠른 수렴속도와 VMC의 최적화 문제 차원감소를

통해서 빠른 시간에 궤적을 생성할 수 있고, 초기 부분 공간 선정에 민감하지 않은 결과를 보여준다.

세 번째로 2 자유도  $H_\infty$  제어기법을 적용하여 불안정하고 유연모드를 가지는 발사체의 자세 제어기를 설계하였다. 자세 제어기 설계 시 충분한 제어이득 여유와 위상 여유를 가지며 응답 속도가 너무 늦지 않도록 하는것을 목표로 하였다. 이를 위해서는 일반적인 강건 제어기의 보수적인 설계 특성을 없애는 것이 무엇보다 중요하다. 우선 기준 제어기로 LQG 와 적분 LQG 제어기를 설계하였다. 이러한 기준 제어기를 통해 가능한 페루프 함수의 여러 특성을 분석 하였다. 특히 최적제어가 적용되었을 때 민감도 함수의 형상을 분석하여 강건 제어기 설계 시 기준으로 삼을 민감도 함수 형상으로 이용하였다. 최적 제어기 분석을 통해 민감도 함수가 교차주파수를 지날 때 완만한 경사를 가지는 것이 성능 향상에 도움을 준다는 것을 확인 하였다. 이를 이용하여 강건 제어기 설계 시 목표 민감도 함수를 저주파수와 교차 주파수에서 다른 기울기를 가지도록 설계를 하여 최적제어의 특성을 강건제어기 설계 시 고려 할 수 있도록 하였다. 위의 결과를 반영하여 피드포워드와 피드백을 함께 이용하는 2 자유도  $H_\infty$  제어기를 설계 하였다. 결과적으로 제안된 제어기는 기존의 단편적인 민감도 함수 형상을 이용한 강건 제어기법에 비해서 덜 보수적인 특성을 가지며 충분한 상대안정도 여유와 응답 속도를 가지는 것을 확인인하였다.

주요어: 발사체, 궤적 최적화 기법, VMC, 강건 제어,  $H_\infty$  control

학 번: 2013-30190